

EMERGENCE OF COMPUTATIONAL STRUCTURE IN A NEURAL NETWORK PHYSICS SIMULATOR

Rohan Hitchcock

University of Melbourne & CSIRO Data61
rhitchcock@student.unimelb.edu.au

Gary W. Delaney

CSIRO Data61
gary.delaney@data61.csiro.au

Jonathan H. Manton

University of Melbourne
jmanton@unimelb.edu.au

Richard Scalzo

CSIRO Data61
richard.scalzo@data61.csiro.au

Jingge Zhu

University of Melbourne
jingge.zhu@unimelb.edu.au

ABSTRACT

Neural networks often have identifiable computational structures — components of the network which perform an interpretable algorithm or task — but the mechanisms by which these emerge and the best methods for detecting these structures are not well understood. In this paper we investigate the emergence of computational structure in a transformer-like model trained to simulate the physics of a particle system, where the transformer’s attention mechanism is used to transfer information between particles. We show that (a) structures emerge in the attention heads of the transformer which learn to detect particle collisions, (b) the emergence of these structures is associated to degenerate geometry in the loss landscape, and (c) the dynamics of this emergence follows a power law. This suggests that these components are governed by a degenerate “effective potential”. These results have implications for the convergence time of computational structure within neural networks and suggest that the emergence of computational structure can be detected by studying the dynamics of network components.

1 INTRODUCTION

Computational structures, by which we mean components of a neural network which perform an interpretable algorithm or task, often emerge in neural networks during training. Understanding how and why these structures form would contribute to making large neural networks more interpretable, and may enable greater control over what is learned and not learned during training. Clear examples of computational structure have been found in large language models (Olsson et al., 2022), vision models (Cammarata et al., 2020) and in toy systems such as Nanda et al. (2023). While some recent progress has been made towards understanding how these emerge (Hoogland et al., 2024; Wang et al., 2024) the mechanism by which this occurs and the best methods for detecting such structures are still open questions.

In this paper we investigate the emergence of computational structure in a transformer-like model for simulating the physics of a system of particles under gravity. During training, computational structures emerge which have a clear connection to the physical laws and driving behaviour of the target system. Specifically we identify certain attention heads that learn collision detection between particles, which we call *collision detection heads*.

Our experiments suggest that the emergence of collision detection behaviour in attention heads coincides with: (a) a change in the head’s training dynamics, and (b) a change in the geometry of the loss landscape near the head’s parameters. For (a) we observe that the correlation between certain features of the data and the attention scores begins to evolve as a power law. For (b) we observe changes in the degeneracy of the loss landscape as measured by the local learning coefficient (Lau et al., 2024). The emergence of a collision detection head is shown in Figure 1. This suggests that the emergence of collision detection heads is governed by a degenerate “effective potential”. The specific contributions of this paper are:

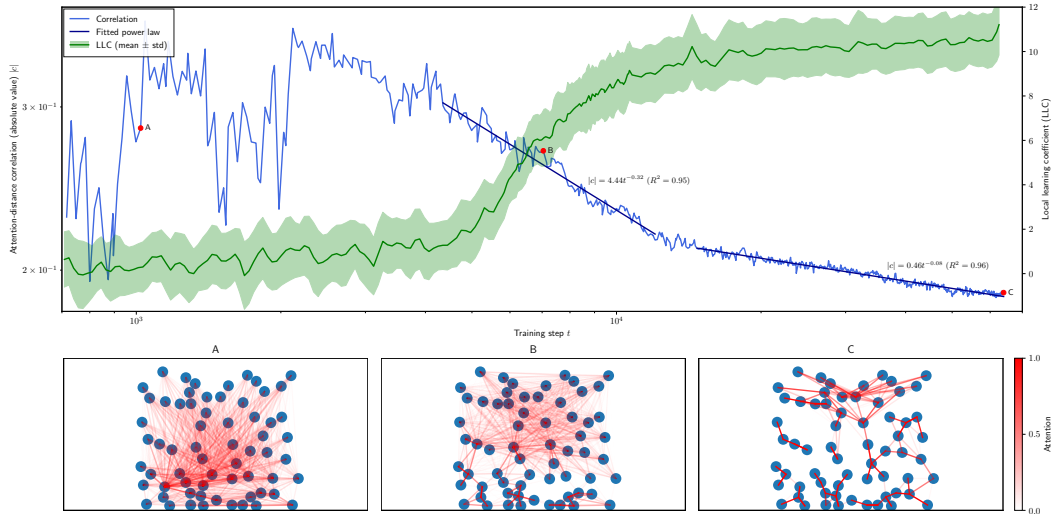


Figure 1: In collision detection heads we see three simultaneous phenomena: collision detection behaviour emerges (bottom), the attention-distance correlation curve enters a power law regime (top, blue) and the local learning coefficient plateaus (top, green). In this head, we see a transition between two distinct phases of collision detection. The behaviour in the first collision detection phase is characterised by collision detection between particles below a certain y -level (bottom, B), as compared to mostly universal collision detection in the second phase (bottom, C). This transition is reflected in the attention-distance correlation curve as different power law exponents, visualised as different slopes on the log-log plot (top, blue). The local learning coefficient plateaus during the first collision detection phase before continuing up to its final value.

- It elicits a connection between degeneracy and computational structure in transformer-like models, and the *dynamics* of these components. This has implications for the convergence time of these components: if they evolve as a power law then structures which form earlier in training will be significantly better formed than those which form later. It also suggests that measurements of the dynamics of model components may be a good way to detect the emergence of computational structure in deep learning models.
- It provides evidence for the role of degeneracy and the formation of computational structures in neural networks trained to simulate physics. The connection here is especially interesting as the phenomena in the model associated with the emergence of collision detection heads (power law behaviour and changes in the degree of degeneracy) are closely connected to *second-order phase transitions* in statistical physics. This interpretation of our results suggests viewing training neural network physics simulators as a coupled system, where the parameters of the network are coupled to the dynamics of the target system.

A running theme through this paper is the effect of degenerate critical points on dynamics and the associated emergence of power laws. We give a self-contained exposition of this in Appendix A.

1.1 RELATED WORK

1.1.1 THE ROLE OF DEGENERACY IN LEARNING

Complex learning machines like neural networks have *degeneracy* in the form of degenerate critical points (saddle points or local minima at which the Hessian is singular) in the loss landscape or log-likelihood function. The importance of this degeneracy in the Bayesian setting has been well-understood for some time (Watanabe, 2009). In strictly singular models (including all non-trivial neural network architectures) the minima of the log-likelihood function are degenerate and non-isolated. Watanabe (2009) showed that the degenerate geometry of this log-likelihood function, in particular the *real log canonical threshold* (RLCT) (see Watanabe, 2009, Definition 2.1), determine much of the learning behaviour of strictly singular models.

These ideas have recently been applied to neural networks trained using stochastic gradient methods. Lau et al. (2024) establishes the *local learning coefficient* (LLC) as a way to quantify the degeneracy in the loss landscape and proposes a method for estimating the LLC. The LLC is derived from results in the Bayesian setting and under certain conditions it coincides with a RLCT (Lau et al., 2024).

The LLC has been applied to study transformers trained on natural language and on a synthetic in-context regression task (Hoogland et al., 2024; Wang et al., 2024). The LLC is shown to identify periods, or *phases*, of training where the model has qualitatively different behaviour. There are similar results in toy models (Chen et al., 2023) and in deep linear networks (Lau et al., 2024).

Separately, distinct phases of training have also been identified by considering the emergence of components of neural networks which perform a certain algorithm. These emergent computational structures are often termed *circuits*, and they have been identified in models such as large language models (Olsson et al., 2022), vision models (Cammarata et al., 2020) and in toy models trained to do modular addition (Nanda et al., 2023). In Hoogland et al. (2024) the emergence of certain circuits in language models is shown to coincide with changes in the local geometry of the loss landscape as measured by the LLC.

1.1.2 STATISTICAL MECHANICS AS A FRAMEWORK FOR UNDERSTANDING LEARNING

Statistical mechanics has been used as a theoretical framework to understand statistical inference and learning; see for example the reviews and textbooks Nishimori (2001); Mezard & Montanari (2009); Zdeborová & Krzakala (2016); Bahri et al. (2020); Huang (2021). Ideas from statistical mechanics have been applied to neural networks in early work Seung et al. (1992); Watkin et al. (1993) and more recently Choromanska et al. (2015); Geiger et al. (2019); Mei et al. (2018); Spigler et al. (2019). When applied to neural networks many of these ideas do not fully account for the degenerate nature of the loss landscape.

Analogies with statistical mechanics are clear in the approach of Watanabe (2009) and are drawn-out in LaMont & Wiggins (2019). Analysis of Bayesian learning in Watanabe (2009) is organised around the concept of the *free energy* of a statistical model applied to a learning task. This is analogous to the concept of the same name from statistical mechanics. A deep theoretical result in Watanabe (2009) is an asymptotic expansion of the free energy in terms of the RLCT of the log-likelihood function.

1.1.3 LEARNED PARTICLE SIMULATION

The transformer-like architecture we use here is similar to a graph neural network, particularly a graph attention based architecture (Veličković et al., 2018; Brody et al., 2022). Graph neural networks (though not using graph attention) have been used to simulate particle systems in Mei et al. (2022); Zhang et al. (2023); Li et al. (2023); Choi & Kumar (2024). Graph neural networks have also been used to simulate other physical systems such as in Sanchez-Gonzalez et al. (2020).

Other than graph neural network approaches, convolutional methods have also been used to learn interactions between particles. Lu et al. (2021); Mital & Andrade (2022) train models based on a convolutional layer originally conceived in Ummenhofer et al. (2020) for fluid simulation. Lai et al. (2022) considers fully connected networks trained to detect and resolve collisions between pairs of particles with complex shapes.

2 METHOD

We train a model to simulate a system of particles where collisions are governed by damped linear spring dynamics (see Luding, 2008). Given the state of such a particle system, the model is trained to predict the state of the system after some fixed time interval Δt . Repeatedly applying the model to its own output means the fully trained model can be used as a simulator.

2.1 MODEL

Our model architecture is based on a transformer using multihead attention; the main difference is that the attention mechanism is used to transfer information between particles rather than between

elements of a sequence. Full details of the model architecture and training process are given in Appendix C. We completed a total of five training runs with this model.

2.2 UNDERSTANDING THE ROLE OF ATTENTION HEADS

To understand how attention heads contribute to detecting collisions between particles we introduce two measurements of an attention head: the *collision detection score* and the *attention-distance correlation function*.

For a given attention head we define its *collision detection score* as the expected attention the head assigns within a small, fixed radius of each query particle. The collision detection score ranges falls between 0 (for a head that never assigns attention to nearby particles) and 1 (for a head which assigns all of its attention to nearby particles). The distribution of collision detection scores evolving over training is shown in Figure 2.

The collision detection score aims to straightforwardly quantify the tendency of an attention head to detect collisions and is used for classifying whether or not a head has collision detection behaviour. We also visualise a head’s attention pattern for a given particle state by drawing a line between every pair of particles, weighted by the assigned attention score (see Figure 3). These visualisations clearly show when an attention head is detecting particle collisions, and qualitatively agree with the collision detection score.

For each attention head we measure the statistical correlation between its attention scores and the distance between particles. Let $\mathbf{w} \in \mathbb{R}^d$ be the parameters of the neural network (for example at a checkpoint over training) and consider a single fixed attention head within the network. For each pair of particles i and j , let $\alpha_{ij}(\mathbf{w})$ be the attention score assigned by the head to the representation of particle j when updating the representation of particle i . We consider the correlation between $\alpha_{ij}(\mathbf{w})$ and the distance $d_{ij} = \|\mathbf{p}_i - \mathbf{p}_j\|$ between particles i and j . The *attention-distance correlation function* for the given head is

$$c(\mathbf{w}) = \frac{1}{N^2 - N} \sum_{i \neq j} \text{corr}(d_{ij}, \alpha_{ij}(\mathbf{w})).$$

where $\text{corr}(d_{ij}, \alpha_{ij}(\mathbf{w}))$ is computed by taking expectations with respect to the data distribution.

The attention-distance correlation function is inspired by correlation functions in statistical mechanics, which are often able to detect qualitative changes in a physical system’s behaviour. We use the dynamics of $c(\mathbf{w})$ — meaning its behaviour as a function of the training step — as a proxy for the dynamics of a collision detection head (this is discussed further in Section 4.1, see also Corollary A.4). When $c(\mathbf{w})$ is tracked over training we will see that these dynamics can be used to identify collision detection heads.

2.3 THE GEOMETRY OF ATTENTION HEAD WEIGHTS

To understand the geometry of the attention head weights we use a parameter-restricted version of the local learning coefficient (LLC) of Lau et al. (2024). The same method is used to study attention heads in language transformers in Wang et al. (2024).

The LLC at a parameter vector $\mathbf{w} \in \mathbb{R}^d$ is a measurement of the degree of degeneracy of the loss landscape near \mathbf{w} . We give a more detailed exposition of the local learning coefficient in Appendix B.1, but for some intuition the term ‘degeneracy’ is used in the same sense as a degenerate critical point; when \mathbf{w} is a local minimum of the loss function then the LLC will be maximal if the Hessian is non-singular at \mathbf{w} . Smaller values of the LLC indicate that \mathbf{w} is more degenerate minimum, in a sense which is closely related to the real log canonical threshold (a geometric invariant). When at a local minimum, the LLC can also be understood as relating to the rate of volume scaling in the loss landscape: a smaller local learning coefficient means that a greater volume of nearby parameters will achieve the same expected loss within a small tolerance ϵ (see Hoogland & van Wingerden (2023); Lau et al. (2024) for more details).

To understand the geometry of a single attention head we treat all parameters other than those in the attention head as fixed and perform LLC estimation using the method described in Lau et al. (2024); Wang et al. (2024). This lets us understand the geometry of the loss function considered only as a

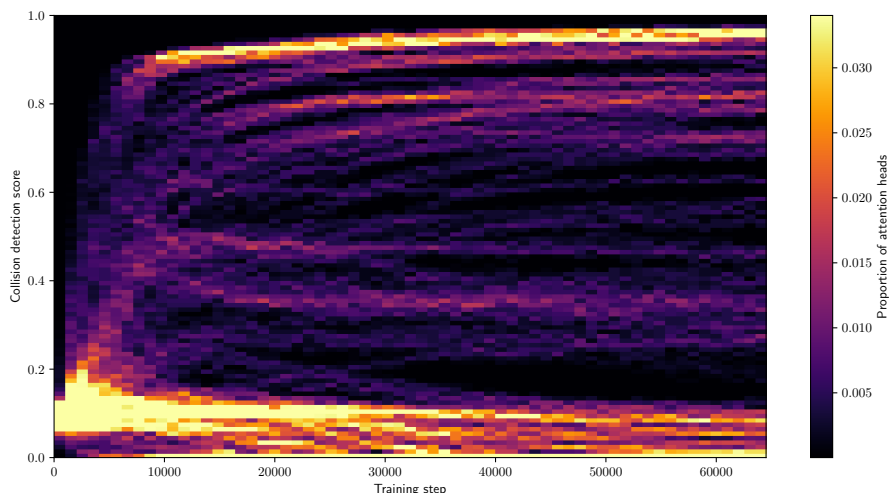


Figure 2: We track the collision detection score for all attention heads over training across all five training runs and aggregate them into a two-dimensional histogram. At the end of training we see a dense cluster of attention heads with collision detection score near 0.95 and a dense cluster near zero, corresponding respectively to true collision detection heads and heads without collision detection behaviour. Between the two large clusters there are several small clusters corresponding to the partial collision detection heads. To improve the dynamic range of this plot, all density values in the 95th percentile are set to the same maximal colour intensity. Versions of this plot showing only the attention heads from a single training run are given in Appendix D.3

function of the parameters of a single attention head. We give specific details about our procedure for estimating the LLC in Appendix B. For heads of interest we estimate the parameter-restricted LLC at many checkpoints over training.

3 RESULTS

Over the course of training we observe that some attention heads learn to detect collisions between particles. We call these heads *collision detection heads*. We study how these collision detection heads develop over training. We observe that in most cases the following occur simultaneously: (a) collision detection behaviour emerges, (b) the attention-distance correlation enters a power law regime, (c) the parameter-restricted local learning coefficient plateaus. These three phenomena are visualised in Figure 1.

3.1 COLLISION DETECTION HEADS

At the end of training we identify attention heads which assign the majority of their attention to particles which are at or near the point of collision, which we call these *collision detection heads*. The distribution of the heads' collision detection scores at the end of training (Figure 2) shows several clusters of heads with similar collision detection scores.

There is a large cluster of heads with a collision detection score of about 0.95, which we refer to as *true collision detection heads*. An example of the attention pattern of a true collision detection head is shown in Figure 3. This visualisation shows that the dominant behaviour¹ of the head is to detect collisions between particles in both particle states. We also have a large cluster of attention heads with collision detection score close to zero which do not exhibit collision detection behaviour. An example attention pattern for such a head is shown in Figure 3.

¹This head has some non-collision detection behaviour among a small group of particles near the top of the system. All true collision detection heads have some degree of anomalous behaviour, often for particles near the top of the system. We don't have a good explanation for why this occurs.

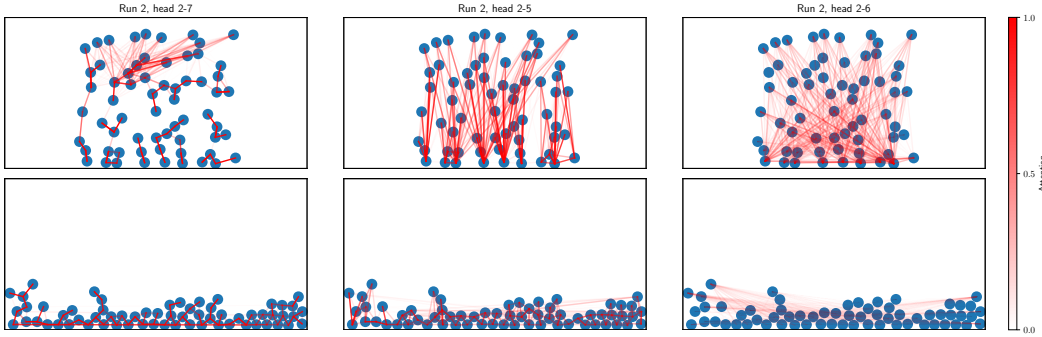


Figure 3: From left to right, examples of a true contact detection head, a partial collision detection head, and a head which is neither. These have collision detection scores 0.95, 0.78 and 0.02 respectively. We show the heads’ behaviour when the particles are in free-fall (top) and when the particles are close to settled (bottom). The attention score assigned by particle i to particle j is indicated by a red line with opacity proportional to the attention score.

In between these two large clusters there are a number of smaller clusters of heads with collision detection score between approximately 0.3 and 0.8. We call these *partial collision detection heads*. Inspecting the attention patterns for heads in these clusters shows that these heads exhibit collision detection behaviour, but only under certain circumstances. For example, the partial collision detection head shown in Figure 3 seems to only detect collisions between particles when the particles are in a settled state.

All training runs develop a mixture of true and partial collision detection heads (see figures in Appendix D.3), and these heads develop in all transformer blocks except the first block (see Figure 5, Appendix D). Additional visualisations of head behaviour are shown in Appendix D.4.

3.2 ATTENTION-DISTANCE CORRELATION POWER LAWS AND THE LLC

We study the development of collision detection heads by looking at how the attention-distance correlation function evolves over training. For collision detection heads the attention-distance correlation evolves as a power law. To see this, we plot the attention-distance correlation $c(\mathbf{w}_t)$ versus the training step t on a log-log plot. Power law sections can be identified as sections of $\log |c|$ vs $\log t$ with a good linear fit. At the end of its development (i.e. at the end of training or before the correlation function stops changing) the correlation function of a collision detection head evolves as a power law (see Figure 1). This occurs in all but six cases. Three of these cases have a ‘power law’ with a positive exponent, and three have no obvious power law behaviour. Of these six anomalous collision detection heads, four appear within the same block for the same training run. There are no attention heads for which the attention-distance correlation follows a power law which are not collision detection heads.

The emergence of power law behaviour in the attention-distance cross-correlation function coincides with changes in the local geometry of the head’s parameters, as measured by the local learning coefficient. We observe that the local learning coefficient plateaus in sections of training where the cross-correlation function is governed by a power law.

3.3 TRANSITIONS BETWEEN HEAD VARIANTS

In the case shown in Figure 1, we observe a head transition between two variants of a collision detection head. Initially a partial collision detection head forms: the head detects collisions between particles only near the lower physical boundary of the particle system as shown in box B. This is associated with the attention-distance correlation function entering a power law regime and the LLC plateauing briefly (note that such plateaus in the LLC do not occur in heads without two power laws; see Appendix D.5). After more training, the head transitions to a true collision detection head (shown in box C) and the attention-distance function moves into a new power law regime with a different

exponent. The LLC also changes and plateaus at a higher level than before. Compared to the LLC, the change in the correlation function’s dynamics has a sharp transition point between the two power law regimes.

4 DISCUSSION

We have shown that collision detection heads — attention heads which detect collisions between particles — develop in a transformer-like model trained to simulate a particle system. This emergence coincides with the attention-distance correlation entering a power law regime and a change in the degeneracy of the head’s parameters as measured by the parameter-restricted local learning coefficient (LLC). We observe at least two variants of collision detection heads, and in one case a head transitioning between these two variants. The transition between these two variants can be identified by a corresponding change in the attention-distance correlation power law exponent and by changes in the LLC. The point of transition is especially clear when observing the power law exponent (see Figure 1). The observed attention-distance correlation power laws and LLC results suggest that the development of collisions detection heads is governed by a degenerate “effective potential”, that this degeneracy results in power law development of collision detection heads, and that transitions between variants of collision detection heads correspond to moving between different effective potentials.

4.1 IMPLIED DYNAMICS OF COLLISION DETECTION HEADS

Power laws are characteristic of a dynamical system which is near a degenerate critical point. The gradient flow of an analytic function can converge at either an exponential or power law rate. Which of these two behaviours it exhibits is characterised by the *Łojasiewicz exponent* $\theta \in [\frac{1}{2}, 1)$ of a nearby critical point; if $\theta = \frac{1}{2}$ then the system converges at an exponential rate, and if $\theta > \frac{1}{2}$ the system converges as a power law with exponent determined by the value of θ . The power law will also show up in measurements of the dynamical system (see Corollary A.4). The Łojasiewicz exponent also characterises a certain kind of degeneracy in critical points, with $\theta = \frac{1}{2}$ if the function is sufficiently non-degenerate (Feehan, 2019). We discuss the Łojasiewicz exponent in more detail in Appendix A.1, along with its relationship to the LLC.

We hypothesise that the observed power law dynamics in the attention-distance correlation function and the corresponding changes in the LLC are explained by a stochastic version of the results discussed above. When a collision detection head forms its development is governed by degenerate critical points in the loss landscape, which we refer to as an “effective potential”. The transition between head variants shown in Figure 1 (and corresponding changes in the LLC and correlation power law) can be explained as the head moving between two different effective potentials with different levels of degeneracy. This hypothesis is consistent with the results of Hoogland et al. (2024) and Chen et al. (2023), which associate the development of certain computational structure with degeneracy in the loss landscape; here we emphasise the effect of this degeneracy on the *dynamics* of the computational structure.

4.2 CONNECTION TO SECOND-ORDER PHASE TRANSITIONS

The emergence of collision detection heads and the associated power laws in many ways resembles a physical system at a second-order phase transition. Power law scaling in various quantities, and in-particular in correlation functions similar to our attention-distance correlation function, is characteristic of a second-order phase transition. These power laws also arise as a result of degenerate critical points, typically in the *free energy* function $f(\omega)$ of a system parameter ω , as we explain in Appendix A.2.

The statistical mechanical interpretation of these results is particularly interesting in the context of training a neural network to simulate physics. Correlation functions in statistical mechanics usually measure the correlation between a quantity measured at two different locations within a physical system. In contrast we measure the correlation between two different quantities, one a measurement of the network and the other a measurement of the target physical system. This suggests viewing training physics simulators as coupled systems, where the neural network is coupled to the target physical system via the training process. While for the model discussed in this paper this is a simple

one-way coupling of the neural network to the target system, more complex couplings are conceivable, such as when training physics models on sequence data or in physics reinforcement learning (see Holl et al., 2020).

4.3 IMPLICATIONS AND FUTURE WORK

These results suggest a description of how computational structure emerges in neural networks more generally; computational structure is associated to degenerate geometry in the loss landscape and, as a result, such structures develop with power law dynamics. Degeneracy in the loss landscape is a feature common to all non-trivial neural networks (see Wei et al., 2022) and it is reasonable to hypothesise that it plays a similar role across different model architectures and learning tasks. This description of how computational structure emerges is consistent with the stagewise development model proposed in Hoogland et al. (2024) and Wang et al. (2024) in the sense that power law dynamics emerge suddenly. However, once a computational component has formed it converges as a power law.

This has implications for the convergence time of computational structures in neural networks. It suggests computational structure develops slowly in the following sense. Consider a quantity $\xi \sim t^{-\alpha}$ converging to zero as a power law in the training step t (for example, ξ is the error in a performance metric of a computational component), and for simplicity take $\alpha = 1$. Halving ξ requires training for twice as long. In contrast if $\xi \sim 2^{-\alpha t}$ is exponential in t (i.e. if the critical point is non-degenerate; see Appendix A.1) halving ξ requires just $\frac{1}{\alpha}$ additional training steps.

A consequence of this is that structures which form earlier in training will be much better formed compared to those which form later, the implication being that promoting the formation of favourable structures and inhibiting the creation of unfavourable ones is particularly important early in training. This may contribute to a partial mechanistic explanation of the results of Achille et al. (2019); Frankle et al. (2020); Chimoto et al. (2024) which demonstrate that early periods of training can be critical in determining the final performance of the network. We emphasise that this is only a partial explanation because we do not consider how the early development of certain structures affects the development of other structures later in training.

Slow convergence of computational structure also suggests that practices like fine-tuning are unlikely to significantly change the computational structures that are present in a model. This is because the training time of fine-tuning is a small proportion of the total training time of the final model. Various works have shown that undesirable behaviour can persist through fine-tuning, or that the changes made by fine-tuning can easily be undone (Hubinger et al., 2024; Zhan et al., 2024; Ji et al., 2024; Qi et al., 2024). Note, however, that the loss landscape is different during the fine-tuning phase of the model and so this topic requires further study.

Our results also have implications for those hoping to detect the emergence of computational structures via measuring degeneracy in the loss landscape. Our results show that the power law dynamics of a computational component become clear well before the local learning coefficient plateaus (Figure 1). The point transition between the two collision detection phases is also sharply resolved by the correlation dynamics, as compared to the LLC curve. While the attention-distance correlation function is specific to this model and training task, it suggests that the measuring the dynamics of network components may be a way of detecting emerging computational structures earlier than the LLC.

4.4 LIMITATIONS

This work studies the emergence of computational structure for a single model; in particular the attention-distance function is specific to this model. While more work is needed to investigate this phenomena in other settings, all non-trivial neural networks have degenerate loss landscapes. The theoretical results relating degeneracy to dynamics surveyed in Appendix A provide good reason to hypothesise that the power law convergence results we observe here should manifest in some form in other settings.

This work only studies the emergence of collision detection heads in isolation and we do not consider how these interact with the rest of the model and the training process. For example we do not consider how the formation of a collision detection head affects the formation of other computational structures in the model later in training.

AUTHOR CONTRIBUTIONS

RH, GWD, JHM, RS, JZ formulated the research question and interpreted the results. RH implemented the methodology, conducted the experiments, analysed the results, and wrote the initial draft of the manuscript. GWD, JHM, RS and JZ provided guidance and advice, and offered critical feedback throughout the study. All authors contributed to the editing and refinement of the manuscript.

ACKNOWLEDGEMENTS

RH was supported by the AI for Missions Scholarship from CSIRO.

REFERENCES

- Achille, A., Rovere, M., and Soatto, S. Critical Learning Periods in Deep Neural Networks, February 2019. URL <http://arxiv.org/abs/1711.08856>.
- Ansel, J., Yang, E., He, H., Gimelshein, N., Jain, A., Voznesensky, M., Bao, B., Bell, P., Berard, D., Burovski, E., Chauhan, G., Chourdia, A., Constable, W., Desmaison, A., DeVito, Z., Ellison, E., Feng, W., Gong, J., Gschwind, M., Hirsh, B., Huang, S., Kalambarkar, K., Kirsch, L., Lazos, M., Lezcano, M., Liang, Y., Liang, J., Lu, Y., Luk, C., Maher, B., Pan, Y., Puhrsch, C., Reso, M., Saroufim, M., Siraichi, M. Y., Suk, H., Suo, M., Tillet, P., Wang, E., Wang, X., Wen, W., Zhang, S., Zhao, X., Zhou, K., Zou, R., Mathews, A., Chanan, G., Wu, P., and Chintala, S. PyTorch 2: Faster Machine Learning Through Dynamic Python Bytecode Transformation and Graph Compilation. In *29th ACM International Conference on Architectural Support for Programming Languages and Operating Systems, Volume 2 (ASPLOS '24)*. ACM, April 2024. doi: 10.1145/3620665.3640366. URL <https://pytorch.org/assets/pytorch2-2.pdf>.
- Bahri, Y., Kadmon, J., Pennington, J., Schoenholz, S. S., Sohl-Dickstein, J., and Ganguli, S. Statistical Mechanics of Deep Learning. *Annual Review of Condensed Matter Physics*, 11(1):501–528, March 2020.
- Brody, S., Alon, U., and Yahav, E. How Attentive are Graph Attention Networks?, January 2022. URL <http://arxiv.org/abs/2105.14491>.
- Cammarata, N., Carter, S., Goh, G., Olah, C., Petrov, M., Schubert, L., Voss, C., Egan, B., and Lim, S. K. Thread: Circuits. *Distill*, 2020. doi: 10.23915/distill.00024.
- Chen, Z., Lau, E., Mendel, J., Wei, S., and Murfet, D. Dynamical versus Bayesian Phase Transitions in a Toy Model of Superposition, October 2023. URL <http://arxiv.org/abs/2310.06301>.
- Chimoto, E. A., Gala, J., Ahia, O., Kreutzer, J., Bassett, B. A., and Hooker, S. Critical Learning Periods: Leveraging Early Training Dynamics for Efficient Data Pruning, June 2024. URL <http://arxiv.org/abs/2405.19462>.
- Choi, Y. and Kumar, K. Graph Neural Network-based surrogate model for granular flows. *Computers and Geotechnics*, 166:106015, February 2024.
- Choromanska, A., Henaff, M., Mathieu, M., Arous, G. B., and LeCun, Y. The loss surfaces of multilayer networks. In *Artificial intelligence and statistics*, pp. 192–204. PMLR, 2015.
- Feehan, P. Resolution of singularities and geometric proofs of the Łojasiewicz inequalities. *Geometry & Topology*, 23(7):3273–3313, December 2019. ISSN 1364-0380, 1465-3060.
- Frankle, J., Schwab, D. J., and Morcos, A. S. The Early Phase of Neural Network Training, February 2020. URL <http://arxiv.org/abs/2002.10365>.
- Geiger, M., Spigler, S., d’Ascoli, S., Sagun, L., Baity-Jesi, M., Biroli, G., and Wyart, M. Jamming transition as a paradigm to understand the loss landscape of deep neural networks. *Physical Review E*, 100(1):012115, July 2019.
- Hartmann, A. K. and Weigt, M. *Phase transitions in combinatorial optimization problems: basics, algorithms and statistical mechanics*. Wiley-VCH, 2005.

- Hironaka, H. Resolution of singularities of an algebraic variety over a field of characteristic zero: II. *Annals of Mathematics*, pp. 205–326, 1964.
- Holl, P., Thuerey, N., and Koltun, V. Learning to control PDEs with differentiable physics. In *International conference on learning representations*, 2020.
- Hoogland, J. and van Wingerden, S. You’re Measuring Model Complexity Wrong, October 2023. URL <https://www.alignmentforum.org/posts/6g8cAftfQufLmFDYT/>.
- Hoogland, J., Wang, G., Farrugia-Roberts, M., Carroll, L., Wei, S., and Murfet, D. The Developmental Landscape of In-Context Learning, February 2024. URL <http://arxiv.org/abs/2402.02364>.
- Huang, H. *Statistical mechanics of neural networks*. Springer, 2021.
- Hubinger, E., Denison, C., Mu, J., Lambert, M., Tong, M., MacDiarmid, M., Lanham, T., Ziegler, D. M., Maxwell, T., Cheng, N., Jermyn, A., Askell, A., Radhakrishnan, A., Anil, C., Duvenaud, D., Ganguli, D., Barez, F., Clark, J., Ndousse, K., Sachan, K., Sellitto, M., Sharma, M., DasSarma, N., Grosse, R., Kravec, S., Bai, Y., Witten, Z., Favaro, M., Brauner, J., Karnofsky, H., Christiano, P., Bowman, S. R., Graham, L., Kaplan, J., Mindermann, S., Greenblatt, R., Shlegeris, B., Schiefer, N., and Perez, E. Sleeper Agents: Training Deceptive LLMs that Persist Through Safety Training, January 2024. URL <http://arxiv.org/abs/2401.05566>.
- Ji, J., Wang, K., Qiu, T., Chen, B., Zhou, J., Li, C., Lou, H., Dai, J., Liu, Y., and Yang, Y. Language Models Resist Alignment: Evidence From Data Compression, December 2024. URL <http://arxiv.org/abs/2406.06144>. arXiv:2406.06144 [cs].
- Lai, Z., Chen, Q., and Huang, L. Machine-learning-enabled discrete element method: Contact detection and resolution of irregular-shaped particles. *International Journal for Numerical and Analytical Methods in Geomechanics*, 46(1):113–140, January 2022.
- LaMont, C. H. and Wiggins, P. A. Correspondence between thermodynamics and inference. *Physical Review E*, 99(5):052140, 2019.
- Lau, E., Furman, Z., Wang, G., Murfet, D., and Wei, S. The Local Learning Coefficient: A Singularity-Aware Complexity Measure, September 2024. URL <http://arxiv.org/abs/2308.12108>.
- Li, Z., Li, X., Zhang, H., Huang, D., and Zhang, L. The prediction of contact force networks in granular materials based on graph neural networks. *The Journal of Chemical Physics*, 158(5):054905, February 2023.
- Lu, L., Gao, X., Dietiker, J.-F., Shahnam, M., and Rogers, W. A. Machine learning accelerated discrete element modeling of granular flows. *Chemical Engineering Science*, 245:116832, December 2021.
- Luding, S. Introduction to discrete element methods: basic of contact force models and how to perform the micro-macro transition to continuum theory. *European journal of environmental and civil engineering*, 12(7-8):785–826, 2008.
- Mei, J., Ma, G., Wang, Q., Wu, T., and Zhou, W. Micro- and macroscopic aspects of the intermittent behaviors of granular materials related by graph neural network. *International Journal of Solids and Structures*, 251:111763, September 2022.
- Mei, S., Montanari, A., and Nguyen, P.-M. A mean field view of the landscape of two-layer neural networks. *Proceedings of the National Academy of Sciences*, 115(33):E7665–E7671, August 2018.
- Mezard, M. and Montanari, A. *Information, physics, and computation*. Oxford University Press, 2009.
- Mital, U. and Andrade, J. E. Bridging length scales in granular materials using convolutional neural networks. *Computational Particle Mechanics*, 9(1):221–235, February 2022.
- Nanda, N., Chan, L., Lieberum, T., Smith, J., and Steinhardt, J. Progress measures for grokking via mechanistic interpretability, January 2023. URL <http://arxiv.org/abs/2301.05217>.

- Nishimori, H. *Statistical Physics of Spin Glasses and Information Processing*. Oxford University Press, 2001.
- Olsson, C., Elhage, N., Nanda, N., Joseph, N., DasSarma, N., Henighan, T., Mann, B., Askell, A., Bai, Y., Chen, A., Conerly, T., Drain, D., Ganguli, D., Hatfield-Dodds, Z., Hernandez, D., Johnston, S., Jones, A., Kernion, J., Lovitt, L., Ndousse, K., Amodei, D., Brown, T., Clark, J., Kaplan, J., McCandlish, S., and Olah, C. In-context Learning and Induction Heads. *Transformer Circuits Thread*, 2022.
- Phuong, M. and Hutter, M. Formal Algorithms for Transformers, July 2022. URL <http://arxiv.org/abs/2207.09238>.
- Qi, X., Zeng, Y., Xie, T., Chen, P.-Y., Jia, R., Mittal, P., and Henderson, P. Fine-tuning aligned language models compromises safety, even when users do not intend to! In *The twelfth international conference on learning representations*, 2024.
- Samiei, K., Peters, B., Bolten, M., and Frommer, A. Assessment of the potentials of implicit integration method in discrete element modelling of granular matter. *Computers & Chemical Engineering*, 49:183–193, February 2013.
- Sanchez-Gonzalez, A., Godwin, J., Pfaff, T., Ying, R., Leskovec, J., and Battaglia, P. Learning to simulate complex physics with graph networks. In *International conference on machine learning*, pp. 8459–8468. PMLR, 2020.
- Seung, H. S., Sompolinsky, H., and Tishby, N. Statistical mechanics of learning from examples. *Physical Review A*, 45(8):6056, 1992.
- Spigler, S., Geiger, M., d’Ascoli, S., Sagun, L., Biroli, G., and Wyart, M. A jamming transition from under- to over-parametrization affects generalization in deep learning. *Journal of Physics A: Mathematical and Theoretical*, 52(47):474001, November 2019.
- Strogatz, S. H. *Nonlinear dynamics and chaos: with applications to physics, biology, chemistry, and engineering*. Westview Press, 2 edition, 2015.
- Tuley, R., Danby, M., Shrimpton, J., and Palmer, M. On the optimal numerical time integration for Lagrangian DEM within implicit flow solvers. *Computers & Chemical Engineering*, 34(6): 886–899, June 2010.
- Ummenhofer, B., Prantl, L., Thuerey, N., and Koltun, V. Lagrangian Fluid Simulation with Continuous Convolutions. In *International Conference on Learning Representations*, 2020.
- van Wingerden, S., Hoogland, J., and Wang, G. Devinterp, 2024. URL <https://github.com/timaeus-research/devinterp>.
- Veličković, P., Cucurull, G., Casanova, A., Romero, A., Liò, P., and Bengio, Y. Graph Attention Networks, February 2018. URL <http://arxiv.org/abs/1710.10903>.
- Wang, G., Hoogland, J., Wingerden, S. v., Furman, Z., and Murfet, D. Differentiation and Specialization of Attention Heads via the Refined Local Learning Coefficient, October 2024. URL <http://arxiv.org/abs/2410.02984>.
- Watanabe, S. *Algebraic geometry and statistical learning theory*. Cambridge University Press, 2009.
- Watanabe, S. A widely applicable Bayesian information criterion. *The Journal of Machine Learning Research*, 14(1):867–897, 2013.
- Watkin, T. L. H., Rau, A., and Biehl, M. The statistical mechanics of learning a rule. *Reviews of Modern Physics*, 65(2):499–556, April 1993.
- Wei, S., Murfet, D., Gong, M., Li, H., Gell-Redman, J., and Quella, T. Deep learning is singular, and That’s good. *IEEE Transactions on Neural Networks and Learning Systems*, 2022.
- Welling, M. and Teh, Y. W. Bayesian learning via stochastic gradient Langevin dynamics. In *Proceedings of the 28th international conference on machine learning (ICML-11)*, pp. 681–688, 2011.

- Yeomans, J. M. *Statistical mechanics of phase transitions*. Oxford University Press, 1992.
- Zdeborová, L. and Krzakala, F. Statistical physics of inference: Thresholds and algorithms. *Advances in Physics*, 65(5):453–552, 2016.
- Zhan, Q., Fang, R., Bindu, R., Gupta, A., Hashimoto, T., and Kang, D. Removing RLHF Protections in GPT-4 via Fine-Tuning, April 2024. URL <http://arxiv.org/abs/2311.05553>.
- Zhang, H., Li, X., Li, Z., Huang, D., and Zhang, L. Estimation of Particle Location in Granular Materials Based on Graph Neural Networks. *Micromachines*, 14(4):714, March 2023.
- Łojasiewicz, S. Sur le probleme de la division. *Studia Mathematica*, 18(1):87–136, 1959.
- Łojasiewicz, S. Une propriété topologique des sous-ensembles analytiques réels. *Les équations aux dérivées partielles*, 117:87–89, 1963.
- Łojasiewicz, S. Triangulation of semi-analytic sets. *Annali della Scuola Normale Superiore di Pisa-Scienze Fisiche e Matematiche*, 18(4):449–474, 1964.
- Łojasiewicz, S. Ensembles semi-analytiques. *Lectures Notes IHES (Bures-sur-Yvette)*, 1965.

A POWER LAWS AND DEGENERACY

In this section we explain how power laws arise from degenerate critical points. This is intended to be expository; none of the results discussed in this section are new to this paper. We give proofs when they are not easily found in the literature.

In Appendix A.1 we define the Łojasiewicz exponent of a critical point and explain how its value characterises the rate of convergence of a corresponding gradient flow. In Appendix A.1.1 we explain the relationship between the Łojasiewicz exponent and degeneracy. In particular we discuss its relationship with the real log canonical threshold, as this is an important quantity in Bayesian learning and closely related to the local learning coefficient. In Appendix A.2 we discuss power laws in statistical mechanics. Using the Ising model as an example, we explain how these also arise from degenerate critical points.

A.1 POWER LAWS IN DYNAMICAL SYSTEMS WITH DEGENERATE POTENTIALS

Whether or not a dynamical system exhibits power law behaviour is determined by the value of the *Łojasiewicz exponent* of a nearby critical point. For an analytic function, the Łojasiewicz exponent θ of a local minimum is a value in $[\frac{1}{2}, 1)$; if $\theta = \frac{1}{2}$ then a gradient flow $\mathbf{x}(t)$ starting sufficiently close to that local minimum will converge at an exponential rate, and if $\theta > \frac{1}{2}$ then $\mathbf{x}(t)$ will converge as a power law.

Let $U \subseteq \mathbb{R}^d$ be an open set and $f : U \rightarrow \mathbb{R}$ be an analytic function. Consider a critical point $\mathbf{x}^* \in U$ of f . To simplify the discussion suppose that $f(\mathbf{x}) \geq f(\mathbf{x}^*)$ for all $\mathbf{x} \in U$, and if $\nabla f(\mathbf{x}) = 0$ then $f(\mathbf{x}) = f(\mathbf{x}^*)$. Let $Z = \{\mathbf{x} \in U \mid f(\mathbf{x}) = f(\mathbf{x}^*)\}$ be the set of minima of f in U . In order to define the Łojasiewicz exponent we need to state the following theorem, which is due to Łojasiewicz (1959; 1963; 1964; 1965).

Theorem A.1 (Łojasiewicz inequalities). *There exist constants $\theta \in [\frac{1}{2}, 1)$ and $C, C' > 0$ and an open neighbourhood V of \mathbf{x}^* such that:*

1. $\|\nabla f(\mathbf{x})\| \geq C|f(\mathbf{x}) - f(\mathbf{x}^*)|^\theta$ for all $\mathbf{x} \in V$.
2. $|f(\mathbf{x}) - f(\mathbf{x}^*)| \geq C'd(\mathbf{x}, Z)^{\frac{1}{1-\theta}}$ for all $\mathbf{x} \in V$.

where $d(\mathbf{x}, Z) = \inf\{\|\mathbf{x} - \mathbf{y}\| \mid \mathbf{y} \in Z\}$ is the distance between \mathbf{x} and Z .

Definition A.2 (Łojasiewicz exponent). Let θ_0 be the smallest value of θ satisfying (1) in Theorem A.1. That is, θ_0 is the infimum of all the $\theta \in [\frac{1}{2}, 1)$ such that there exists a neighbourhood V of \mathbf{x}^* and $C > 0$ satisfying

$$\|\nabla f(\mathbf{x})\| \geq C|f(\mathbf{x}) - f(\mathbf{x}^*)|^\theta \text{ for all } \mathbf{x} \in V.$$

We call θ_0 the *Łojasiewicz exponent* of \mathbf{x}^* .

The Łojasiewicz exponent characterises the rate at which a gradient flow of f — that is, a solution to $\mathbf{x}'(t) = -\nabla f(\mathbf{x}(t))$ — converges to the critical point \mathbf{x}^* . When the Łojasiewicz exponent $\theta_0 = \frac{1}{2}$ the gradient flows converge exponentially quickly to Z , and when $\theta_0 > \frac{1}{2}$ they converge as a power law.

Corollary A.3. *Let $\mathbf{x}(t)$ be a gradient flow of f starting sufficiently close to \mathbf{x}^* and $\theta \in [\frac{1}{2}, 1)$ be any value such that inequalities (1) and (2) in Theorem A.1 hold. Then:*

1. If $\theta = \frac{1}{2}$ then $d(\mathbf{x}(t), Z) \leq Ae^{-at}$ for all t , for some constants $A, a > 0$.
2. If $\theta > \frac{1}{2}$ then $d(\mathbf{x}(t), Z) \leq A(t + B)^{-\alpha}$ for all t , where $\alpha = \frac{1-\theta}{2\theta-1} > 0$ and A, B are constants, $A > 0$.

Proof. Without loss of generality suppose that $\mathbf{x}^* = \mathbf{0}$ and $f(\mathbf{x}^*) = 0$. Define $F(t) = f(\mathbf{x}(t))$, and note that

$$F'(t) = \nabla f(\mathbf{x}(t)) \cdot \mathbf{x}'(t) = -\|\nabla f(\mathbf{x}(t))\|^2.$$

When $\theta = \frac{1}{2}$ we have

$$-F'(t) \geq CF(t).$$

for some $C > 0$ by Theorem A.1. Rearranging (recall that we have assumed $f(\mathbf{x}) \geq f(\mathbf{x}^*) = 0$) and integrating both sides gives

$$-\int_0^t \frac{F'(s)}{F(s)} ds \geq Ct$$

Computing the integral and rearranging again gives

$$F(t) \leq Ae^{-a't}$$

for some $A, a' > 0$. Applying inequality 2 from Theorem A.1 gives the desired result.

For $\theta > \frac{1}{2}$ we instead consider

$$\begin{aligned} F(t)^{1-2\theta} &= \int_0^t \frac{d}{ds} (F(s)^{1-2\theta}) ds + F(0)^{1-2\theta} \\ &= \int_0^t (1-2\theta)F'(s)F(s)^{-2\theta} ds + D \\ &= (2\theta-1) \int_0^t \|\nabla f(\mathbf{x}(s))\|^2 f(\mathbf{x}(s))^{-2\theta} ds + D \end{aligned}$$

where $D = F(0)^{1-2\theta}$. Theorem A.1 gives

$$\begin{aligned} F(t)^{1-2\theta} &\geq (2\theta-1) \int_0^t C f(\mathbf{x}(s))^{2\theta} f(\mathbf{x}(s))^{-2\theta} ds + D \\ &\geq A't + D \end{aligned}$$

where $A' = (2\theta-1)C > 0$. Rearranging and applying inequality 2 from Theorem A.1 gives the desired result. \square

In our results in the main paper, however, we do not observe power laws in a distance function, but rather in some other measurement of our system. The following corollary shows that when $\mathbf{x}(t)$ converges as a power law, so does any sufficiently nice scalar measurement $Q(\mathbf{x}(t))$.

Corollary A.4. *Let $Q : U \rightarrow \mathbb{R}$ be β -Hölder continuous function and let $\mathbf{x}(t)$ be a gradient flow of f starting sufficiently close to \mathbf{x}^* . Let $\theta \in [\frac{1}{2}, 1)$ be any value such that inequalities (1) and (2) in Theorem A.1 hold, and $Q^* = \lim_{t \rightarrow \infty} Q(\mathbf{x}(t))$. Then for some $T \in \mathbb{R}$ sufficiently large*

1. *If $\theta = \frac{1}{2}$ then $|Q(\mathbf{x}(t)) - Q^*| \leq A'e^{-\alpha\beta t}$ for all $t > T$.*
2. *If $\theta > \frac{1}{2}$ then $|Q(\mathbf{x}(t)) - Q^*| \leq A'(t + B')^{-\alpha\beta}$ for all $t > T$,*

where a, α and B are the constants from Corollary A.3 and $A' > 0$.

Proof. Recall that Q being β -Hölder continuous means that for all $\mathbf{x}, \mathbf{y} \in U$

$$|Q(\mathbf{x}) - Q(\mathbf{y})| \leq C'\|\mathbf{x} - \mathbf{y}\|^\beta$$

for some $C' > 0$. Let $\mathbf{z} = \lim_{t \rightarrow \infty} \mathbf{x}(t)$. Since Z is a closed set we have $\mathbf{z} \in Z$, and also there exists a T such that for all $t > T$ we have $d(\mathbf{x}(t), \mathbf{z}) = d(\mathbf{x}(t), Z)$. Combining the inequalities in Corollary A.3 and the inequality from Q being Hölder continuous yields the desired result.

Note that a slight variation on this argument shows that if $Q(\mathbf{z}) = Q^*$ for all $\mathbf{z} \in Z$ then the stated inequalities hold for all t where $\mathbf{x}(t)$ is defined. \square

Example A.5 (see Strogatz 2015, Chapter 3.4). Consider the function $f : \mathbb{R} \rightarrow \mathbb{R}$ where $f(x) = \frac{r}{2}x^2 + \frac{1}{4}x^4$ and $r \in \mathbb{R}$ is a constant. The corresponding gradient flow equation is

$$x'(t) = -rx(t) - x(t)^3. \quad (1)$$

For $r \geq 0$ the function f has a single critical point: a global minimum at $x = 0$. When $r < 0$ the function f has three critical points: a local maximum at $x = 0$ and two local minima located symmetrically about $x = 0$. When $r \neq 0$ the critical points are all non-degenerate, but when $r = 0$

the critical point $x = 0$ is degenerate. For $r \neq 0$ we have $x'(t) \approx -rx(t)$ in a neighbourhood of $x = 0$. Solving this approximate version of the differential equation gives

$$|x(t)| \approx Ae^{-rt}$$

for some $A > 0$ depending on the initial conditions. When $r = 0$ we instead solve $x'(t) = -x(t)^3$ to obtain

$$|x(t)| = \frac{1}{\sqrt{2}}(t + B)^{-\frac{1}{2}}$$

where B depends on the initial conditions. We can use the exponent $\alpha = \frac{1}{2}$ to find an *ansatz* for the Łojasiewicz exponent. We solve $\frac{1}{2} = \frac{1-\theta_0}{2\theta_0-1}$ to obtain $\theta_0 = \frac{3}{4}$. The first Łojasiewicz inequality in Theorem A.1 for $x^* = 0$ becomes

$$|x^3| \geq C|\frac{1}{4}x^4|^\theta.$$

Setting $C = 4$ and $\theta = \frac{3}{4}$ we obtain equality for all $x \in \mathbb{R}$. From this it is straightforward to prove that the Łojasiewicz exponent of $f(x) = \frac{1}{4}x^4$ is $\frac{3}{4}$.

A.1.1 RELATIONSHIP TO DEGENERACY

The Łojasiewicz exponent characterises a certain kind of degeneracy in critical points. When the critical point is sufficiently non-degenerate the Łojasiewicz exponent is equal to $\frac{1}{2}$. Specifically, if the function f is *Morse-Bott* then the Łojasiewicz exponent of any critical point of f is equal to $\frac{1}{2}$ (Feehan, 2019, Theorem 2.1). A function is Morse-Bott if its set of critical points form a manifold and the Hessian of f is non-degenerate in directions normal to this critical manifold. Put another way, the set of critical points of an analytic function f is in-general an analytic set which may have singularities, and the condition of being Morse-Bott means that the set of critical points of f does not have singularities. Combining with the results discussed in Corollary A.3, this means that power law behaviour is characteristic of a function f with singularities in its set of critical points. In the Bayesian learning context (i.e. when f is the log-likelihood function of a statistical model) the condition of being Morse-Bott corresponds to the case that the statistical model is *minimally singular*.

Another measurement of degeneracy relevant to us is the *real log canonical threshold* (RLCT) (see Watanabe, 2009, Definition 2.7). The RLCT is relevant because it is closely related to the local learning coefficient (their relationship is discussed in Lau et al. (2024, Appendix A) and also in Appendix B). The RLCT characterises non-degeneracy in the same way as the Łojasiewicz exponent: if f is Morse-Bott then the RLCT of its set of critical points is maximal. For a function f which is not Morse-Bott the relationship between the RLCT and the Łojasiewicz exponent is complex and, to the best of the authors' knowledge, not fully understood.

An interesting result related to the Łojasiewicz exponent is that of Feehan (2019, Theorem 3) which proves the Łojasiewicz inequalities for an analytic function in *normal crossing form* (see Feehan, 2019, Definition 1.1), and hence for all analytic functions via Hironaka's resolution of singularities theorem (Hironaka, 1964); a statement of this theorem is also given in Watanabe (2009, Theorem 2.3)). A consequence of this result is an upper bound for the Łojasiewicz exponent of f in terms of properties of a resolution of singularities of f . Normal crossing functions and resolution of singularities are key components of the proof in Watanabe (2009) that the RLCT of the log-likelihood function is an important quantity in Bayesian learning.

A.2 POWER LAWS IN STATISTICAL PHYSICS

Power laws are characteristic of statistical mechanical systems at second order phase transitions. In this section we explain, using the example of the Ising model on a fully connected graph, that these power laws arise for the same reason as power laws in dynamical systems: degenerate critical points in a certain function. For the necessary background on statistical mechanics and phase transitions we refer readers to Yeomans (1992); Hartmann & Weigt (2005).

A.2.1 EXAMPLE: THE ISING MODEL ON A FULLY CONNECTED GRAPH

We consider the Ising model on a fully connected graph with N nodes. This example is adapted from Hartmann & Weigt (2005, Chapter 5.3), and is considered primarily because it is one of the few cases

where calculations can be done explicitly. A state of this system is a vector $\boldsymbol{\sigma} = (\sigma_1, \dots, \sigma_N)$ where $\sigma_i \in \{-1, +1\}$ is the value at node i . The system is governed by the Hamiltonian

$$H(\boldsymbol{\sigma}) = -\frac{1}{N} \sum_{i < j} \sigma_i \sigma_j - h \sum_{i=1}^N \sigma_i$$

where $h \in \mathbb{R}$ is a hyperparameter of the system. States are distributed according to the Boltzmann distribution

$$p(\boldsymbol{\sigma}) = \frac{1}{Z} \exp(-\beta H(\boldsymbol{\sigma})) \quad \text{where} \quad Z = \sum_{\boldsymbol{\sigma}'} \exp(-\beta H(\boldsymbol{\sigma}'))$$

where $\beta > 0$ is another hyperparameter.

We consider the behaviour of this system in the limit as $N \rightarrow \infty$. Physically speaking, the Ising model is a simplified model of magnetism in a solid. The nodes represent a small volume of the solid, which are magnetised in one of two polarities (“spin up” $\sigma_i = +1$, or “spin down” $\sigma_i = -1$). The magnetisation of a particular state $\boldsymbol{\sigma}$ is given by the average of these values

$$m(\boldsymbol{\sigma}) = \frac{1}{N} \sum_{i=1}^N \sigma_i.$$

We can rewrite the Hamiltonian as a function of the magnetisation $m := m(\boldsymbol{\sigma})$ like so

$$H(m) = -\frac{N}{2} m^2 - hNm + \frac{1}{2}.$$

The hyperparameter h represents an external magnetic field, and $1/\beta$ is the thermal temperature of the solid. This system has phase transitions in (h, β) where the expected magnetisation $\mathbb{E}[m(\boldsymbol{\sigma})]$ changes suddenly as the h and β are varied. For fixed $\beta > 1$ the system has a phase transition at $h = 0$ where the expected magnetisation changes sign to align with h . Physically this corresponds to the solid magnetising with the same polarity as the external magnetic field. This is a first-order phase transition. More interestingly, when $h = 0$ the system has a phase transition at $\beta = 1$, where $\mathbb{E}[|m(\boldsymbol{\sigma})|]$ changes from a non-zero value for $\beta > 1$ to $\mathbb{E}[|m(\boldsymbol{\sigma})|] = 0$ for $\beta < 1$. Unlike in the previous case, where $\mathbb{E}[m(\boldsymbol{\sigma})]$ was discontinuous as a function of f , only the derivatives of $\mathbb{E}[m(\boldsymbol{\sigma})]$ with respect to h and β are discontinuous (see Yeomans, 1992, Figure 2.1). Physically this corresponds to the Curie point of a material, where a magnet suddenly becomes demagnetised once it is heated past a certain temperature. The point $(h, \beta) = (0, 1)$ is a second order phase transition of the system. For more details on the phase structure of the Ising model see Yeomans (1992, Chapter 2).

We can understand these phase transitions by studying the partition function Z or equivalently the free energy $F = -\frac{1}{\beta} \log(Z)$. This is because the expected magnetisation is a derivative of the free energy

$$\mathbb{E}[m(\boldsymbol{\sigma})] = \frac{-1}{N} \frac{\partial F}{\partial h}.$$

We now consider the partition function Z . For large N one can show

$$Z \approx \int_{-1}^1 \exp(-\beta N f(m)) dm$$

where

$$\beta f(m) = \frac{1}{2} \beta m^2 + hm - \frac{1+m}{2} \log\left(\frac{1+m}{2}\right) - \frac{1-m}{2} \log\left(\frac{1-m}{2}\right)$$

For details of this derivation see Hartmann & Weigt (2005, Chapter 5.3). Incidentally, $f(m)$ is (approximately, for large N) the free energy of a state with magnetisation m

$$f(m) \approx \frac{1}{N} H(m) - \frac{1}{\beta} \log(\mathcal{N}(m))$$

where $\mathcal{N}(m)$ is the number of states with magnetisation m , and so $\log(\mathcal{N}(m))$ is the entropy.²

²Our definition of Ising model implicitly sets units so that the Boltzmann constant $k_B = 1$.

For large N we can approximate Z using a saddle point approximation

$$Z \approx \exp(-\beta N f(m^*) + \mathcal{O}(\log N))$$

where m^* is an isolated global minimum³ of $f(m)$. The derivative of $f(m)$ is

$$f'(m) = \frac{1}{\beta} \operatorname{arctanh}(m) - m - h$$

where $\operatorname{arctanh}$ is the inverse to \tanh . Solving $f'(m) = 0$ lets us find m^* . This is best done graphically using the methods described in Strogatz (2015, Chapter 3). We focus on the two interesting cases of $h = 0$ and $\beta < 1$ and $h = 0$ and $\beta > 1$. In the former we have a single solution $m = 0$ which is a local minimum. In the latter we have three solutions: two local minima $m = \pm M(\beta)$ for some $M(\beta) \in \mathbb{R}$, and a local maximum at $m = 0$. Note that the $m = 0$ changes from a local minima as β is varied past $\beta = 1$.

We now show that in a neighbourhood of $m = 0$ and $\beta = 1$ the system $f'(m) = 0$ resembles that of Example A.5. Rearranging we find

$$0 = \tanh(\beta m) - m .$$

In a neighbourhood of $m = 0$ we can use the Taylor expansion of $\tanh(\beta m)$ to obtain

$$0 \approx \beta m - \beta^3 m^3 .$$

Setting $T = \frac{1}{\beta}$ (the temperature), the critical value is $T_c = 1$. We define $r = \frac{T - T_c}{T_c} = T - 1$, which gives $\beta = \frac{1}{r+1}$. In a neighbourhood of $r = 0$ we have $\beta \approx 1 - r$. Substituting this approximation and dropping the higher order terms we find

$$0 \approx -rm - m^3 .$$

Note the similarities with (1) in Example A.5. Writing m in terms of r we find the power law relationship

$$|m| \sim |r|^{\frac{1}{2}}$$

when m is in a neighbourhood of $m = 0$ and r is in a neighbourhood of $r = 0$. Other power laws exist in a neighbourhood of this critical point and are discussed in Yeomans (1992, Chapter 2.6).

A.2.2 LIMITATIONS IN THE ANALOGY TO DEEP LEARNING

While the above example is instructive, there is an important difference with the nature of the critical points encountered in the Ising model and similar statistical mechanical systems and those encountered in deep learning. In Appendix A.2.1 we relied on a saddle point approximation of Z . For this to be valid this required that the critical points of $f(m)$ were isolated. For neural networks this is not the case and a more careful treatment is required, such as the approach developed in Watanabe (2009, Chapter 4). We emphasise however that the results discussed in Appendix A.1 do not depend on critical points being isolated and so we should still have an expectation of power law behaviour in a neighbourhood of sets of non-isolated critical points.

B LOCAL LEARNING COEFFICIENT ESTIMATION

In this section we give an overview of the theoretical and practical aspects of estimating the local learning coefficient. In Appendix B.1 we explain the formulation of the local learning coefficient via a specially constructed Bayesian posterior distribution. Nothing discussed in Appendix B.1 is original to this paper: the connection between Bayesian learning and degenerate geometry is a deep result established in Watanabe (2009) with estimation methods first proposed in Watanabe (2013). The specialisation of these results to local (as opposed to global) geometry and to deep learning is due to Lau et al. (2024); Chen et al. (2023).

In Appendix B.2 we discuss the details of the local learning coefficient estimation results in this paper, including the estimation hyperparameters and details of the hyperparameter selection process and additional results.

³The validity of this saddle point approximation depends on $f(m)$ having isolated global minima. We have not shown this is the case, but it does.

B.1 THEORETICAL FORMULATION

In this section consider a neural network $f : \mathbb{R}^N \times W \rightarrow \mathbb{R}^M$ which takes inputs in \mathbb{R}^N , outputs in \mathbb{R}^M and has parameters $W \subseteq \mathbb{R}^d$. Let $q(\mathbf{x}, \mathbf{y})$ be a distribution on $\mathbb{R}^N \times \mathbb{R}^M$ and $D_n = \{(X_1, Y_1), \dots, (X_n, Y_n)\}$ be a dataset of input-output pairs drawn independently from $q(\mathbf{x}, \mathbf{y})$. We consider the task of training the neural network using the mean-squared error loss function:

$$\ell(\mathbf{w}, \mathbf{x}, \mathbf{y}) = \|\mathbf{y} - f(\mathbf{x}, \mathbf{w})\|^2$$

The goal is find parameters which minimise the expected loss

$$L(\mathbf{w}) = \mathbb{E}_{(X,Y) \sim q(\mathbf{x}, \mathbf{y})} \ell(\mathbf{w}, X, Y). \quad (2)$$

Formally speaking, local learning coefficient estimation amounts to computing the expectation with respect to a Bayesian posterior. For a given parameter $\mathbf{w}_0 \in W$ (for example a training checkpoint of our neural network), we construct a Bayesian learning problem which is distinct from, but related to, the problem of training our neural network on the given task. Our Bayesian learning problem is constructed in such a way that it tells us something about the local geometry of $L(\mathbf{w})$ near the parameter \mathbf{w}_0 ; if \mathbf{w}_0 happens to be a local minimum it specifically tells about degeneracy of \mathbf{w}_0 as a critical point of $L(\mathbf{w})$. That Bayesian learning can tell us anything about the degeneracy of critical points is a deep theoretical result established in Watanabe (2009; 2013).

For a given parameter $\mathbf{w}_0 \in W$ a Bayesian learning problem is constructed as follows. We choose a (small) compact neighbourhood $W' \subseteq W$ of \mathbf{w}_0 and a prior $\varphi(\mathbf{w})$ with support W' .⁴ Assume that the input distribution $q(\mathbf{x})$ is known; the learning problem is to recover the true conditional distribution $q(\mathbf{y} | \mathbf{x})$ derived from $q(\mathbf{x}, \mathbf{y})$. For each $\mathbf{w} \in W$ we define a conditional distribution

$$p(\mathbf{y} | \mathbf{x}, \mathbf{w}) \propto \exp(-\frac{1}{2}\|\mathbf{y} - f(\mathbf{x}; \mathbf{w})\|^2).$$

This definition is chosen so that the negative log-likelihood of $p(\mathbf{y} | \mathbf{x}, \mathbf{w})$ as a function of \mathbf{w} coincides with the expected loss $L(\mathbf{w})$ in (2). Define

$$W'_0 = \{\mathbf{w} \in W' \mid L(\mathbf{w}) = L_0\} \quad \text{where } L_0 = \min_{\mathbf{w} \in W'} L(\mathbf{w}).$$

Subject to some technical assumptions (see Lau et al., 2024, Appendix A), including that $L(\mathbf{w})$ is an analytic function of W , the *real log canonical threshold* (RLCT) of the analytic variety W'_0 — which we denote $\lambda(W'_0)$ — can be estimated using Watanabe (2013, Theorem 4) as

$$\hat{\lambda}(W'_0) := n\beta \left(\mathbb{E}_{\mathbf{w}}^{(\beta)} [L_n(\mathbf{w})] - L_n(\mathbf{w}_0) \right) \quad (3)$$

where $L_n(\mathbf{w}) = \frac{1}{n} \sum_{i=1}^n \ell(\mathbf{w}, X_i, Y_i)$, $\beta > 0$ and $\mathbb{E}_{\mathbf{w}}^{(\beta)}$ denotes expectation with respect to the tempered Bayesian posterior distribution at inverse temperature β :

$$p^{(\beta)}(\mathbf{w} | D_n) \propto \varphi(\mathbf{w}) \exp(-\beta n L_n(\mathbf{w})). \quad (4)$$

If \mathbf{w}_0 is a global minimum of $L(\mathbf{w})$ on W' and a further technical assumption is met (roughly speaking that \mathbf{w}_0 is the most degenerate critical point of $L(\mathbf{w})$ in W' in the sense measured by the RLCT) then $\lambda(W'_0)$ coincides with the local RLCT of \mathbf{w}_0 as a critical point of $L(\mathbf{w})$ (Lau et al., 2024, Appendix A).

Estimating the local learning coefficient in (3) amounts to sampling from the tempered posterior distribution in (4). This is done using Markov-chain Monte Carlo methods, specifically the Stochastic Gradient Langevin Dynamics (SGLD) algorithm (Welling & Teh, 2011) which uses minibatches of the dataset D_n to compute each update rather than the entire dataset. For practical reasons a sharp Gaussian prior centred at \mathbf{w}_0

$$\varphi(\mathbf{w}) \propto \exp(-\frac{\gamma}{2}\|\mathbf{w} - \mathbf{w}_0\|^2) \quad \text{where } \gamma > 0$$

is used rather than a prior with compact support. Here γ is a hyperparameter of the local learning coefficient estimation procedure. Starting at \mathbf{w}_0 SGLD generates a sequence of parameters $\mathbf{w}_0, \mathbf{w}_1, \mathbf{w}_2, \dots, \mathbf{w}_T$ where $\mathbf{w}_{t+1} = \mathbf{w}_t + \Delta \mathbf{w}_t$ and

$$\Delta \mathbf{w}_t = -\frac{\epsilon}{2}(\gamma(\mathbf{w} - \mathbf{w}_0) + n\beta \nabla L_m(\mathbf{w}_t)) + \eta_t(\epsilon) \quad (5)$$

⁴In practice however $\varphi(\mathbf{w})$ is chosen to be a sharp Gaussian prior which does not have compact support.

where $\epsilon > 0$ is the step size, m is the batch size and $\eta_t(\epsilon) \sim \text{Normal}(\mathbf{0}, \epsilon I)$ are iid for $t = 0, \dots, T-1$. After a burn-in period of B steps, the expectation $\mathbb{E}_{\mathbf{w}}^{(\beta)}[L_n(\mathbf{w})]$ is approximated as

$$\mathbb{E}_{\mathbf{w}}^{(\beta)}[L_n(\mathbf{w})] \approx \frac{1}{T-B} \sum_{t=B}^T L_m(\mathbf{w}_t).$$

B.2 EMPIRICAL DETAILS

In this paper we consider *weight restricted* local learning coefficient estimation, in which all parameters in a model are considered fixed except for those within a certain architectural component of the model (in our case an attention head). This lets us focus on the geometry of specific components of our model, rather than how the geometry changes as a function of all trainable parameters. In the notation of Appendix B.1 this amounts to choosing our parameter space W to consist only of the parameters of a given attention head, with the remainder of the parameters of the model fixed for the purpose of estimating the local learning coefficient.

As described in Appendix B.1, we estimate the local learning coefficient using SGLD using components of the `devinterp` Python library (van Wingerden et al., 2024). Referring to the update rule of SGLD given in (5), the hyperparameters of the estimation procedure are the step size $\epsilon > 0$, the localisation strength $\gamma > 0$, the batch size m , the number of steps T , the number of burn-in steps B , and the gradient factor $\tilde{\beta} := n\beta$. Since our training data can be generated as-needed from a ground truth physics simulation we generate a sufficiently large dataset so that samples are never reused by SGLD. When producing the LLC results in Figure 1 and Appendix D.5 we complete C independent estimation runs — or chains — at each training checkpoint. We also apply a small amount of smoothing to these LLC curves by taking averages over a small, fixed-width sliding window. The hyperparameters used to obtain our main local learning coefficient results are given in Table 1.

Table 1: Hyperparameters for local learning coefficient results.

HYPERPARAMETER	VALUE
STEP SIZE ϵ	0.00075
LOCALISATION γ	1
GRADIENT FACTOR $\tilde{\beta}$	1385
BATCH SIZE m	256
TOTAL STEPS T	10000
BURN-IN STEPS B	9000
NUMBER OF CHAINS C (FIGURE 1)	8
NUMBER OF CHAINS C (APPENDIX D.5)	4

B.2.1 HYPERPARAMETER SELECTION PROCESS

Hyperparameters were chosen by inspecting the *trace plots* of different SGLD runs. The trace plot of a sequence of SGLD steps $\mathbf{w}_0, \mathbf{w}_1, \dots, \mathbf{w}_T$ is the graph of the step t versus the loss $L_m(\mathbf{w}_t)$. Healthy trace plots should show that $L_m(\mathbf{w}_t)$ converges to fluctuate around a fixed positive value as t becomes large, and should be free from pathologies like large spikes and erratic fluctuations. Sweeps were conducted over ϵ , γ and $\tilde{\beta}$, where the batch size m and total steps T were increased as-needed based on observations from previous sweeps. The number of burn-in steps B was chosen so that the loss trace had converged. For each set of hyperparameters SGLD was performed at a number of checkpoints over training with the goal of finding a single set of hyperparameters which worked well over all training checkpoints.

Finding hyperparameters that worked for both earlier and later checkpoints was a particular challenge. The loss trace for earlier checkpoints tended to converge much slower. Normally this could be resolved by increasing the learning rate, but this caused divergence in later checkpoints. This was resolved by increasing the batch size m to be four times greater than the batch size used during training (this allowed the later checkpoints to tolerate a higher learning rate) and increasing the total

number of steps T . Even still, we could not find a single set of hyperparameters which worked for all collision detection heads over all training checkpoints.

C MODEL AND TRAINING DETAILS

In this section we give the details of the model architecture, training process and training data generation. Figure 4 shows a detailed diagram of the model architecture and Table 4 summarises the model’s hyperparameters. To specify physical boundaries we use virtual ‘boundary particles’ with positions $\mathbf{b}_1, \dots, \mathbf{b}_M \in \mathbb{R}^D$. These do not have a velocity and are not moved by collisions with the particles in the system.

We trained this model architecture for 64000 steps on input-output pairs of states, where the output state is $\Delta t = 0.005$ after the input state. Training hyperparameters are given in Table 2.

The training data is generated as follows. A D -dimensional particle state with N particles is a tensor $\mathbf{x} = [\mathbf{p} \ \mathbf{v}] \in \mathbb{R}^{N \times 2D}$ consisting of the positions $\mathbf{p} \in \mathbb{R}^{N \times D}$ and velocity $\mathbf{v} \in \mathbb{R}^{N \times D}$ of every particle in the system. We randomly initialise a particle state $\mathbf{x}_0 = [\mathbf{p}_0 \ \mathbf{v}_0]$ in a fixed rectangular box and then simulate it for 1024 steps using damped linear spring dynamics to resolve collisions between particles (Luding (2008); see Table 3 for the simulation hyperparameters). The number of steps was chosen as after this point the particle system has generally dissipated all of its energy and particles are no longer moving. The resulting sequence of states $\mathbf{x}_0, \mathbf{x}_1, \dots, \mathbf{x}_{1024}$ is then turned into input-output pairs $(\mathbf{x}_0, \mathbf{x}_1), (\mathbf{x}_1, \mathbf{x}_2), \dots, (\mathbf{x}_{1023}, \mathbf{x}_{1024})$. This process is then repeated for a different random initial state. Samples from multiple sequences are shuffled together before training. We generate enough training data so that the model never sees the same data sample more than once.

Table 2: Hyperparameters for training process.

HYPERPARAMETER	VALUE
OPTIMISER	ADAM
LEARNING RATE	0.001
WEIGHT DECAY	0
BATCH SIZE	64
NUMBER OF TRAINING STEPS	64000
NUMBER OF RUNS	5

Table 3: Hyperparameters for data generation.

HYPERPARAMETER	VALUE
SPATIAL DIMENSION D	2
NUMBER OF PARTICLES N	64
PARTICLE DIAMETER	1
PARTICLE MASS	1
TIME STEP Δt	0.005
COLLISION SPRING CONSTANT	1000
COLLISION DAMPING COEFFICIENT	10
ACCELERATION DUE TO GRAVITY $\ \mathbf{g}\ $	9.8
BOX HEIGHT	14
BOX WIDTH	28
INITIAL PARTICLE VELOCITY DISTRIBUTION	STANDARD NORMAL
NUMBER OF SIMULATED STEPS FROM INITIAL STATE	1024

C.1 MODEL ARCHITECTURE

The model architecture is summarised in Figure 4 and we describe its components in more detail below. The values of hyperparameters of the architecture are given in Table 4. The input data of the model consists of the states of N particles, each of which has a position $\mathbf{p}_i \in \mathbb{R}^D$ and a velocity

$\mathbf{v}_i \in \mathbb{R}^D$. We also have the positions of B boundary particles $\mathbf{b}_1, \dots, \mathbf{b}_B \in \mathbb{R}^D$. These are virtual particles used to indicate the presence of physical barriers in the system and they are densely placed along physical boundaries in the system.

Table 4: Hyperparameters for model architecture.

HYPERPARAMETER	VALUE
NUMBER OF BLOCKS L	4
NUMBER OF HEADS	8
EMBEDDING DIMENSION E	128
BOUNDARY MASK RADIUS r	2
ACTIVATION FUNCTION σ	RELU

Embedding The state of each particle $\mathbf{x}_i = [\mathbf{p}_i \ \mathbf{v}_i] \in \mathbb{R}^{2D}$ is passed through two fully-connected layers $\mathbf{x}_i \mapsto \mathbf{x}'_i := W_{e2}\sigma(W_{e1}\mathbf{x}_i + \mathbf{c}_{e1}) + \mathbf{c}_{e2}$ to obtain the *embedded particle state* $\mathbf{x}'_i \in \mathbb{R}^E$. Here $W_{e1} \in \mathbb{R}^{E \times 2D}$, $W_{e2} \in \mathbb{R}^{E \times E}$, $\mathbf{c}_{e1}, \mathbf{c}_{e2} \in \mathbb{R}^E$ and σ is the activation function. Separately, for each particle we do a graph convolution to include information about nearby boundaries. For each particle i we compute the *embedded boundary data* $\mathbf{b}'_i \in \mathbb{R}^E$

$$\mathbf{b}'_i = \sum_{j=1}^B \mathbf{1}(\|\mathbf{p}_i - \mathbf{b}_j\| < r) [W_{b2}\sigma(W_{b1}\mathbf{b}_j + \mathbf{c}_{b1}) + \mathbf{c}_{b2}]$$

where $\mathbf{1}(\|\mathbf{p}_i - \mathbf{b}_j\| < r)$ is the *radial mask*, selecting only the boundary particles within r units of the current particle, and $W_{b1} \in \mathbb{R}^{E \times D}$, $W_{b2} \in \mathbb{R}^{E \times E}$, $\mathbf{c}_{b1}, \mathbf{c}_{b2} \in \mathbb{R}^E$. This embedded boundary data is then used to update the embedded particle state:

$$\mathbf{x}_i^{(0)} = \mathbf{x}'_i + \mathbf{b}'_i.$$

Transformer blocks The embedded state of each particle is then passed through L transformer blocks. The main components of each block are the multihead attention layer and the two-layer MLP. Layer normalisation is also used as indicated in Figure 4. In the multihead attention layer each particle attends to the other embedded particle states to update its own embedding. Every particle is allowed to attend to every particle embedding other than its own. The multihead attention layer is almost the same as in Phuong & Hutter (2022, Algorithm 5) with one modification which means that the total attention assigned by a particle can be less than one. This is done by appending the zero vector to the key and value vectors before the attention scores are implemented. See the implementation of the `add_zero_attn` option of `MultiheadAttention` in PyTorch (Ansel et al., 2024). The MLP layer operates on each particle embedding and consists of two fully-connected layers separated by a non-linearity.

Unembedding After the transformer blocks and an additional layer normalisation step, the final embedding of each particle state $\mathbf{x}_i^{(L)}$ is projected to a vector $\mathbf{a}_i \in \mathbb{R}^D$ using a single linear layer: $\mathbf{a}_i = W_u \mathbf{x}_i^{(L)} + \mathbf{c}_u$. The updated position \mathbf{p}'_i and velocity \mathbf{v}'_i are obtained by

$$\mathbf{v}'_i = \mathbf{v}_i + \Delta t(\mathbf{a}_i + \mathbf{g}) \quad \mathbf{p}'_i = \mathbf{p}_i + \Delta t \mathbf{v}'_i \quad (6)$$

where $\mathbf{g} \in \mathbb{R}^D$ is acceleration due to gravity. We can interpret the output \mathbf{a}_i of the model as the net acceleration experienced by particle i due to collisions with other particles. With this interpretation, (6) corresponds to integrating the equations of motions using the first-order *semi-implicit Euler method*. When applied to numerical particle simulations this integrator has good stability properties (Samiei et al., 2013; Tuley et al., 2010).

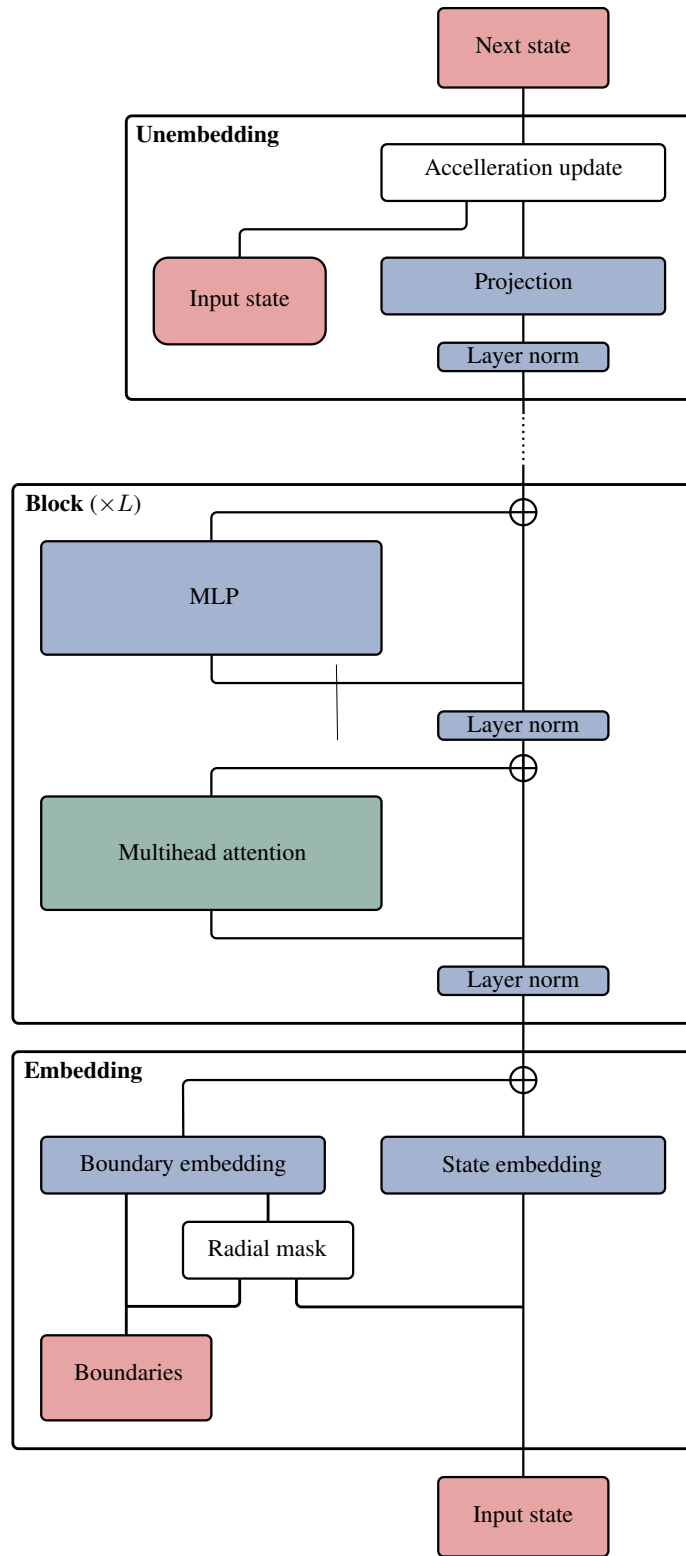


Figure 4: The model architecture. Layers which operate on particle embeddings in-parallel are shaded in blue. Layers which mix information between particle embeddings are shaded in green. Data is shaded in red. Operations without any trainable parameters are left unshaded.

D ADDITIONAL RESULTS AND METHODS

In this section we give some additional results. In Figure 5 we give the number of partial and true collision detection heads, broken down by training run and by location within the network architecture. In Appendix D.1 we give the fitted power laws for all collision detection heads in the model as well as discussing the fitting methodology, in Appendix D.2 we discuss the performance of the model as a particle simulator, in Appendix D.4 we give further visualisations of attention along the lines of Figure 3, and in section Appendix D.5 we give additional attention-distance correlation and local learning coefficient results, with plots similar to Figure 1 produced for other collision detection heads.

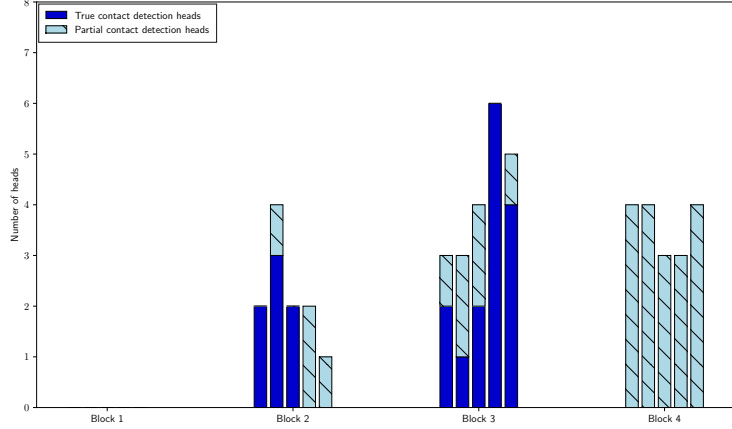


Figure 5: The number of true collision detection heads and partial collision detection heads within each transformer block at the end of training. There are eight attention heads in each block. Data is shown for all five training runs, each as a separate bar.

D.1 POWER LAW FIT STATISTICS

We identified heads where the attention-distance correlation curve $c(t)$ has power law behaviour by inspecting a log-log plot of $|c(t)|$ versus training step t . On a log-log plot a power law $|c| = At^{-\alpha t}$ appears linear. For the heads where power laws were identified we used least-squares linear regression on the transformed plot of $\log(|c|)$ versus $\log(t)$ to find parameters α and A for the curve $\log(|c|) = -\alpha \log(t) + \log(A)$. This corresponds to a power law $|c| = At^{-\alpha}$. We report the power law sections, corresponding fitted parameters, and the R^2 value of the linear fit in Table 5. We also attempt to estimate the error in α by computing a 95% confidence interval for α under the following assumption: the true relationship between $\log(|c|)$ and $\log(t)$ is linear, and the data used to produce the fit has iid normal errors with zero mean. This error term is also reported in Table 5. We plot the power law exponents in Figure 6. This plot shows some clustering of power law exponents near certain values.

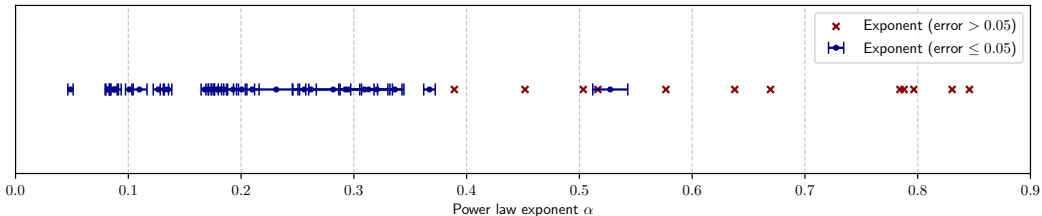


Figure 6: The values of the exponent α in the fitted power law relationship $|c| = At^{-\alpha}$ between the attention-distance correlation c and the training step t . Error bars are omitted from exponents where the estimated error is greater than 0.05 to improve readability.

Table 5: The results from fitting a power law of the form $|c| = At^\alpha$ where c is the attention-distance correlation of the given head and t is training time in steps. To obtain the fit, least-squares linear regression was applied to find parameters $\log(|c|) = \alpha \log(t) + \log(A)$ for t between the given start and end values. The R^2 column is the R^2 value associated to this linear regression. The error term in α indicates the 95% confidence interval for α under the assumption that $\log(|c|)$ and $\log(t)$ have a linear relationship and that the data used to produce the fit have iid normal errors with zero mean.

RUN	HEAD	EXPONENT $-\alpha$	LOG-CONSTANT $\log(A)$	R^2	START STEP	END STEP
0	(1, 4)	-0.784 ± 0.131	5.134	0.934	4864	5734
0	(1, 6)	-0.788 ± 0.128	5.145	0.831	4596	6695
0	(2, 1)	-0.321 ± 0.014	1.491	0.954	4352	12032
0	(2, 1)	-0.082 ± 0.002	-0.771	0.961	14976	64000
0	(2, 5)	-0.179 ± 0.003	0.263	0.964	16000	64000
0	(2, 6)	-0.256 ± 0.004	1.317	0.975	18944	64000
0	(3, 1)	-0.262 ± 0.005	1.363	0.971	22616	64000
0	(3, 2)	-0.087 ± 0.004	-0.711	0.839	24320	64000
0	(3, 3)	-0.313 ± 0.008	1.827	0.950	27392	64000
0	(3, 4)	-0.179 ± 0.006	0.422	0.925	26624	64000
1	(1, 0)	-0.127 ± 0.005	-0.259	0.895	22784	64000
1	(1, 2)	-0.831 ± 0.252	5.107	0.703	2702	3683
1	(1, 6)	-0.503 ± 0.081	2.584	0.884	4804	6272
1	(1, 7)	-0.638 ± 0.076	3.653	0.874	2118	3936
1	(2, 1)	-0.087 ± 0.003	-0.730	0.904	22121	64000
1	(2, 3)	-0.231 ± 0.019	0.879	0.801	32226	47998
1	(2, 6)	-0.185 ± 0.008	0.255	0.907	4992	21636
1	(3, 0)	-0.527 ± 0.016	4.288	0.958	41216	64000
1	(3, 4)	-0.293 ± 0.005	1.777	0.975	20096	64000
1	(3, 6)	-0.210 ± 0.006	0.856	0.932	26368	64000
1	(3, 7)	-0.171 ± 0.003	0.212	0.976	16227	64000
2	(1, 0)	-0.797 ± 0.184	5.535	0.813	6144	7552
2	(1, 1)	-0.846 ± 0.145	5.671	0.893	4397	5609
2	(2, 0)	-0.182 ± 0.006	0.438	0.923	24960	64000
2	(2, 1)	-0.295 ± 0.049	1.096	0.760	8540	12416
2	(2, 5)	-0.336 ± 0.006	2.262	0.971	25856	64000
2	(2, 7)	-0.309 ± 0.023	1.204	0.897	5504	11904
2	(3, 0)	-0.193 ± 0.005	0.574	0.954	28800	64000
2	(3, 1)	-0.175 ± 0.004	0.448	0.947	23168	64000
2	(3, 6)	-0.168 ± 0.003	0.364	0.964	19328	64000
3	(1, 0)	-0.089 ± 0.005	-0.015	0.752	19584	64000
3	(1, 2)	-0.049 ± 0.002	-0.952	0.788	13696	64000
3	(2, 2)	-0.516 ± 0.112	3.240	0.715	8320	11138
3	(2, 4)	-0.389 ± 0.118	1.611	0.525	3584	5994
3	(3, 2)	-0.367 ± 0.005	2.559	0.982	22121	64000
3	(3, 3)	-0.135 ± 0.003	0.405	0.936	15744	64000
3	(3, 6)	-0.101 ± 0.003	-0.505	0.904	22616	64000
4	(2, 1)	-0.452 ± 0.078	2.444	0.833	4397	6265
4	(2, 3)	-0.577 ± 0.111	3.522	0.727	4911	7808
4	(2, 5)	-0.669 ± 0.105	3.983	0.832	2585	4224
4	(2, 7)	-0.282 ± 0.036	1.156	0.731	10752	18944
4	(3, 1)	-0.201 ± 0.005	0.545	0.953	22912	64000
4	(3, 2)	-0.110 ± 0.007	-0.394	0.775	29495	64000
4	(3, 5)	-0.082 ± 0.003	-0.760	0.911	20608	64000
4	(3, 7)	-0.132 ± 0.004	-0.094	0.930	21760	64000

D.2 PERFORMANCE OF THE FULLY TRAINED MODEL AS A PARTICLE SIMULATOR

To verify that the model has actually captured the true physics of the particle system in some way we check that it can be used to simulate a particle system by repeatedly applying the fully-trained model to its own output. For a given initial state $\mathbf{x}_0 \in \mathbb{R}^{N \times 2D}$ we can generate a sequence of states by setting $\mathbf{x}_{n+1} = f(\mathbf{x}_n; \mathbf{w}_{\text{final}})$ where $\mathbf{w}_{\text{final}}$ are the model’s parameters at the end of a training run. Simulations generated in this way appear qualitatively correct compared to results generated by the ground-truth simulator. In Figure 7 we show the total energy at each state in a simulation generated in this way alongside the ground truth, averaged over different initial states. This shows that when the model is used as a simulator the resulting simulations are stable (accumulated errors do not cause the simulation to gain unrealistic amounts of energy) and that on-average the energy evolves in a manner similar to the ground truth system.

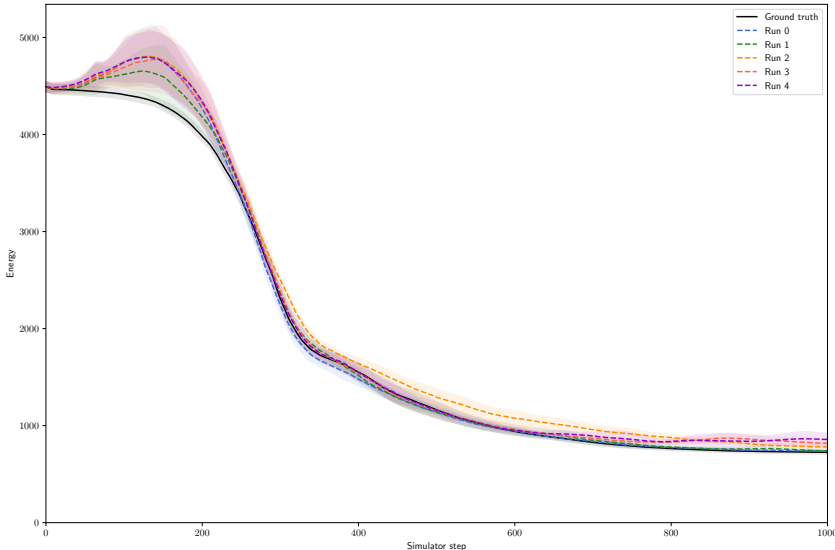


Figure 7: For each run we plot the total energy of the system at each state in a 1000 step simulation, averaged over different initial states. Energy values are presented in reduced units, where a particle’s mass and diameter are taken as the fundamental units of mass and length. This shows that the fully trained models have a similar behaviour to the ground truth system when used as a simulator. The total energy of the system consists of the sum of the kinetic and gravitational potential energy of each particles plus the potential energy stored during collisions between particles.

D.3 ADDITIONAL CONTACT SCORE PLOTS

In Figure 2 we showed the distribution of collision detection scores evolving over training for all attention heads across all five training runs. In this section we present a version of that figure for each of the five training runs individually, where we only show the attention heads from that training run (Figures 8-12). As in Figure 2, we see that in each training run a cluster of heads with a large collision detection score (true collision detection heads), a large cluster of heads with a collision detection score close to zero (heads without collision detection behaviour), and several smaller clusters with intermediate collision detection score (partial collision detection heads). In particular we observe that all training runs develop a mixture of true and partial collision detection heads (see also Figure 5).

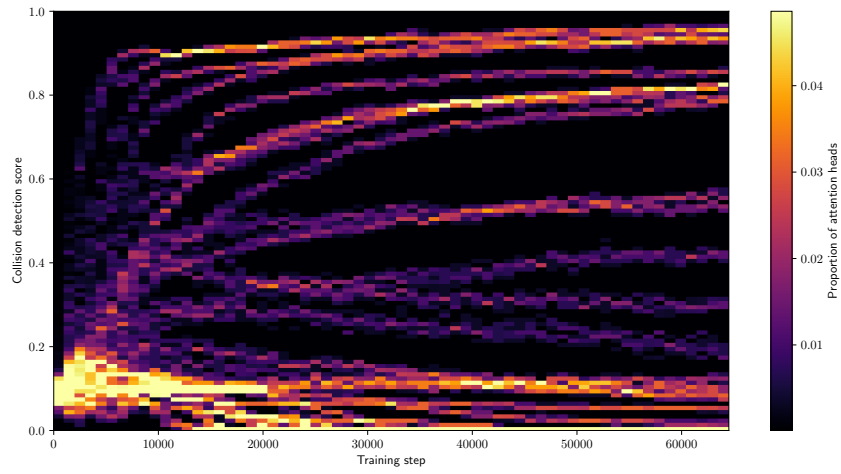


Figure 8: Distribution of collision detection scores of all attention heads for training run 0.

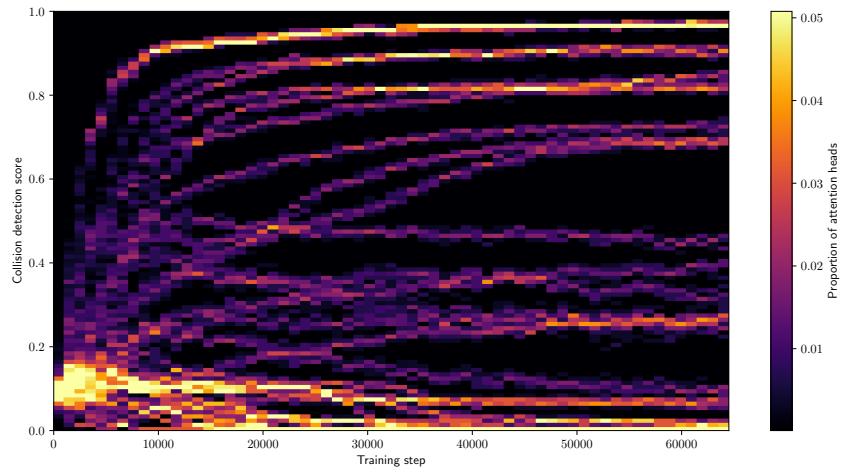


Figure 9: Distribution of collision detection scores of all attention heads for training run 1.

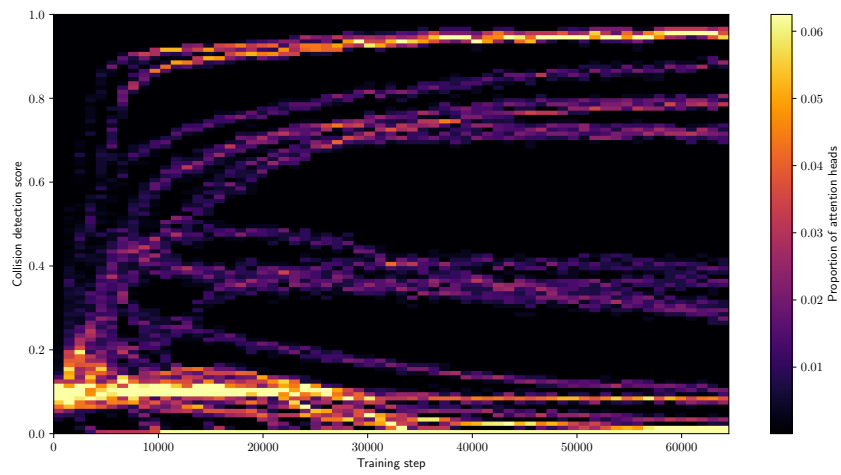


Figure 10: Distribution of collision detection scores of all attention heads for training run 2.

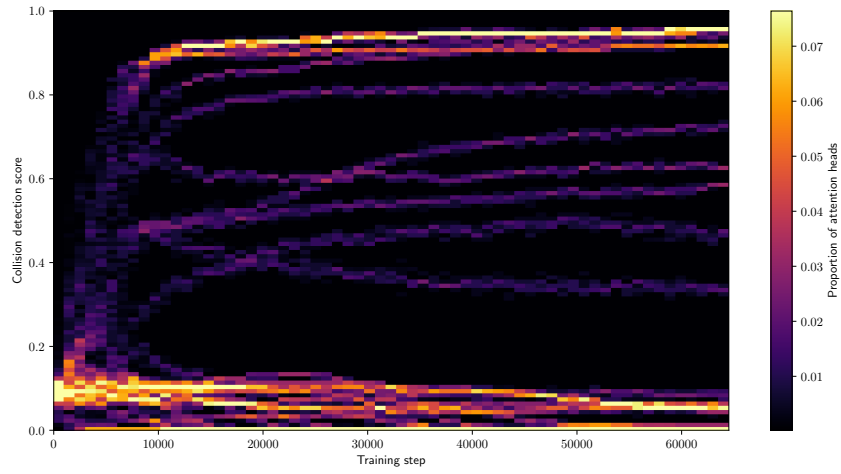


Figure 11: Distribution of collision detection scores of all attention heads for training run 3.

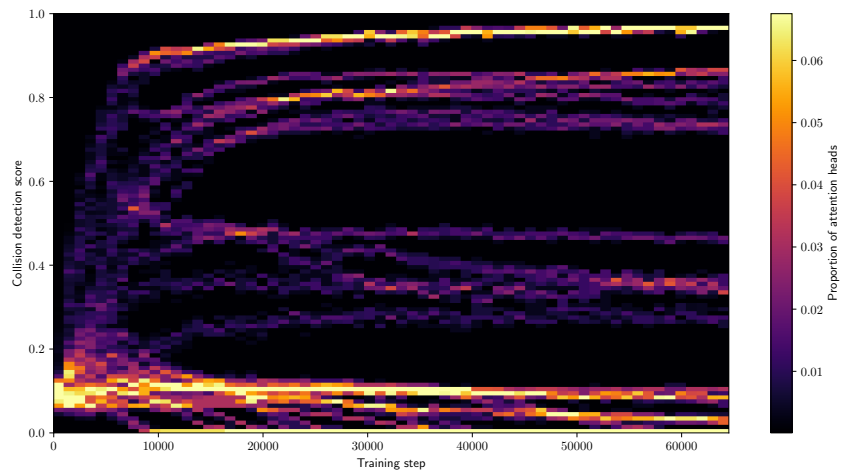


Figure 12: Distribution of collision detection scores of all attention heads for training run 4.

D.4 ADDITIONAL ATTENTION PLOTS

Here we provide more visualisations of attention for the attention heads shown in Figure 3. These figures were produced by moving a single particle around in a given particle state, with all other particles kept in the same positions. We visualise the attention scores for the chosen particle only.

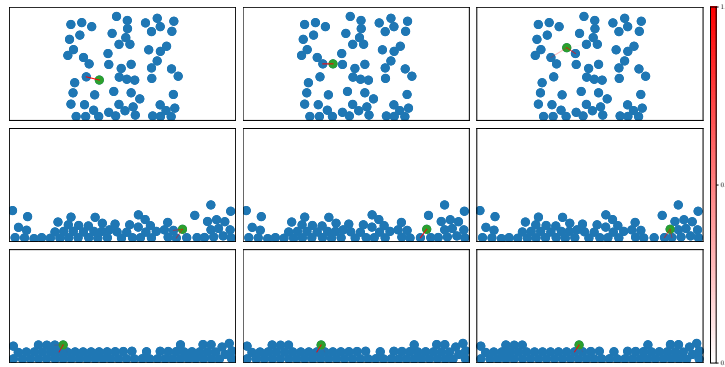


Figure 13: Attention patterns of a single particle (shown in green) for head 2-7 in run 2. This head is a true collision detection head, and is the same head as shown in the left subplot of Figure 3.

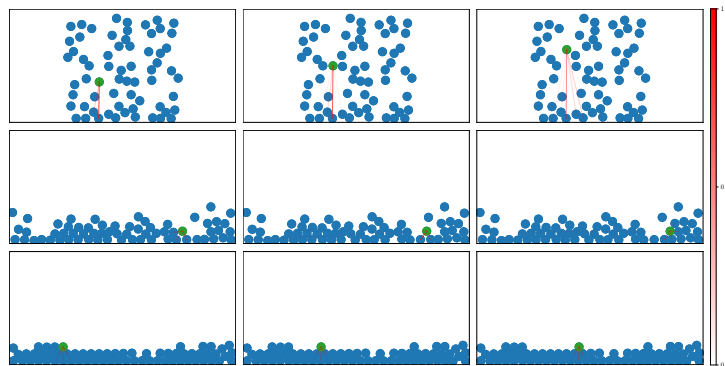


Figure 14: Attention patterns of a single particle (shown in green) for head 2-5 in run 2. This head is a partial collision detection head, and is the same head as shown in the middle subplot of Figure 3.

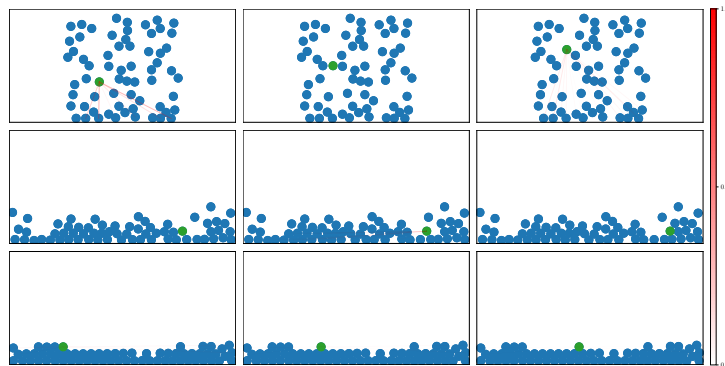


Figure 15: Attention patterns of a single particle (shown in green) for head 2-5 in run 2. This head is not a collision detection head, and is the same head as shown in the right subplot of Figure 3.

D.5 ADDITIONAL CORRELATION AND LOCAL LEARNING COEFFICIENT RESULTS

We give additional attention-distance correlation and local learning coefficient results, similar to Figure 1. So that LLC estimates can be compared we needed to use a single set of LLC estimation hyperparameters (given in Table 1) for all attention heads. It was not possible to find a single set of hyperparameters which produced acceptable trace plots for all heads, for all model checkpoints. For this reason only we only show plots for a subset of the collision detection heads in this section.

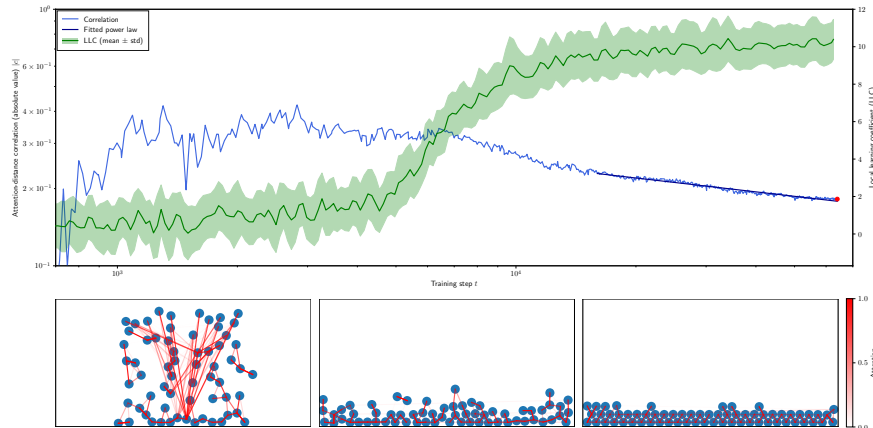


Figure 16: Attention-distance correlation and local learning coefficient results for head 2-5 in training run 0. The fitted curve is $\log(|c|) = -0.179 \log(t) + 0.263$ with $R^2 = 0.961$ (see Table 5).

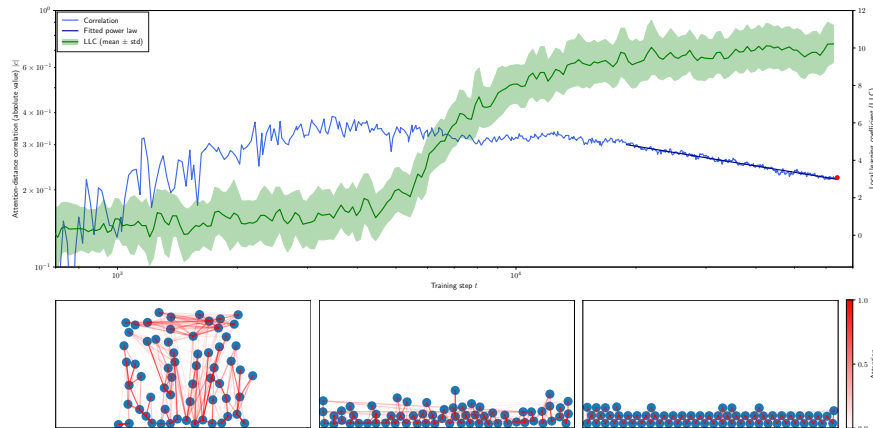


Figure 17: Attention-distance correlation and local learning coefficient results for head 2-6 in training run 0. The fitted curve is $\log(|c|) = -0.256 \log(t) + 1.317$ with $R^2 = 0.975$ (see Table 5).

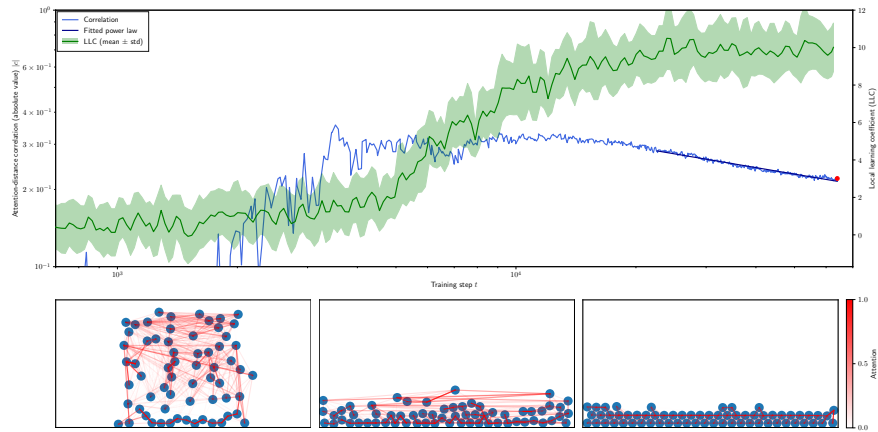


Figure 18: Attention-distance correlation and local learning coefficient results for head 3-1 in training run 0. The fitted curve is $\log(|c|) = -0.262 \log(t) + 1.363$ with $R^2 = 0.971$ (see Table 5).

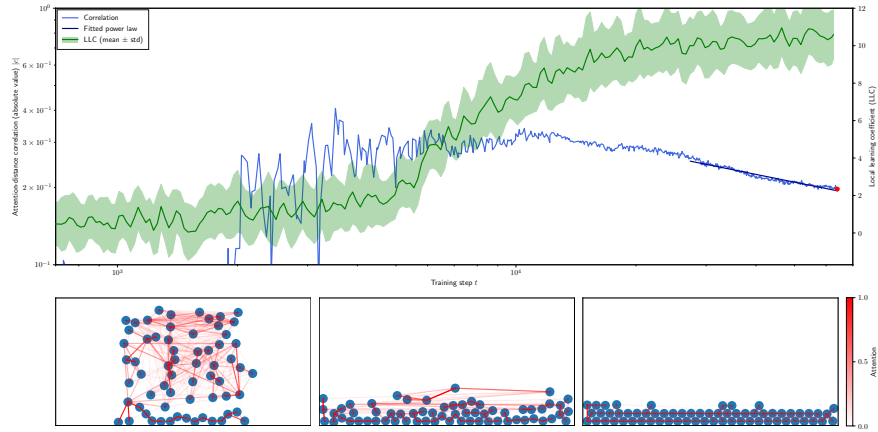


Figure 19: Attention-distance correlation and local learning coefficient results for head 3-3 in training run 0. The fitted curve is $\log(|c|) = -0.313 \log(t) + 1.827$ with $R^2 = 0.950$ (see Table 5).

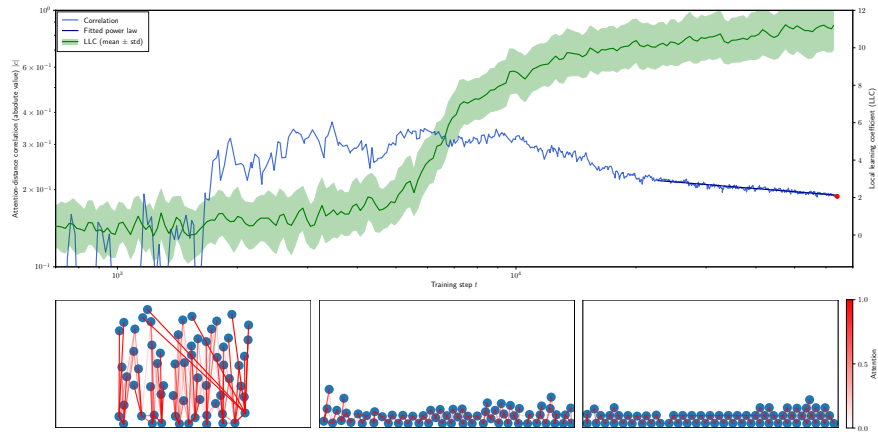


Figure 20: Attention-distance correlation and local learning coefficient results for head 1-0 in training run 1. The fitted curve is $\log(|c|) = -0.127 \log(t) - 0.259$ with $R^2 = 0.895$ (see Table 5).

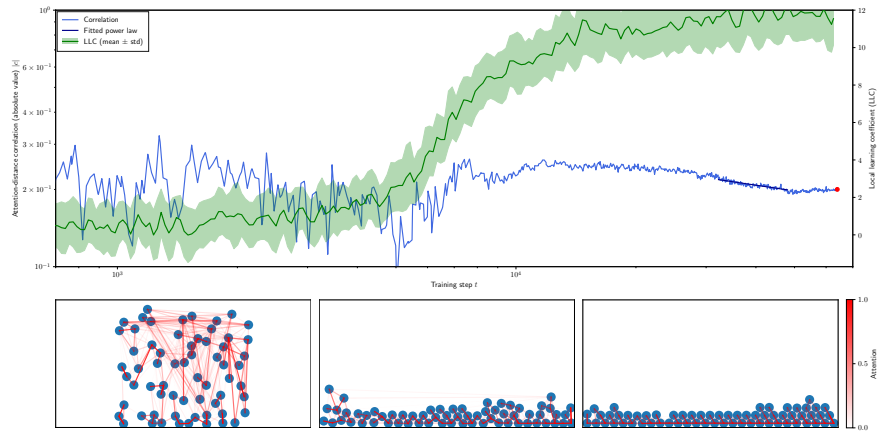


Figure 21: Attention-distance correlation and local learning coefficient results for head 2-3 in training run 1. The fitted curve is $\log(|c|) = -0.231 \log(t) + 0.879$ with $R^2 = 0.801$ (see Table 5).

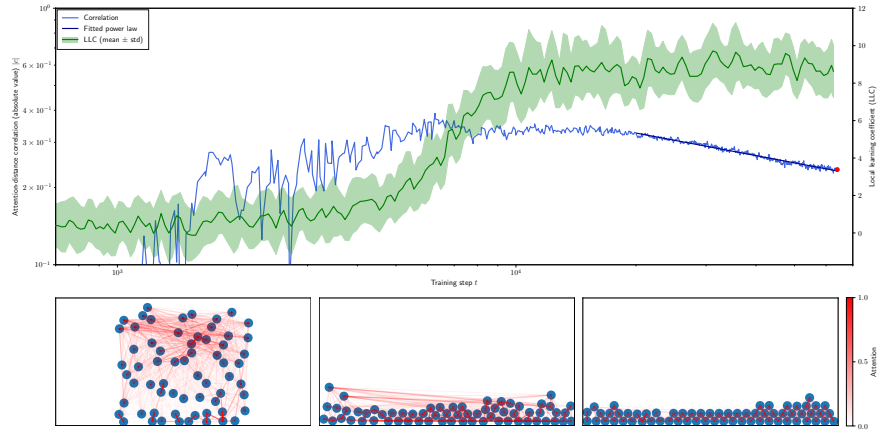


Figure 22: Attention-distance correlation and local learning coefficient results for head 3-4 in training run 1. The fitted curve is $\log(|c|) = -0.293 \log(t) + 1.777$ with $R^2 = 0.975$ (see Table 5).

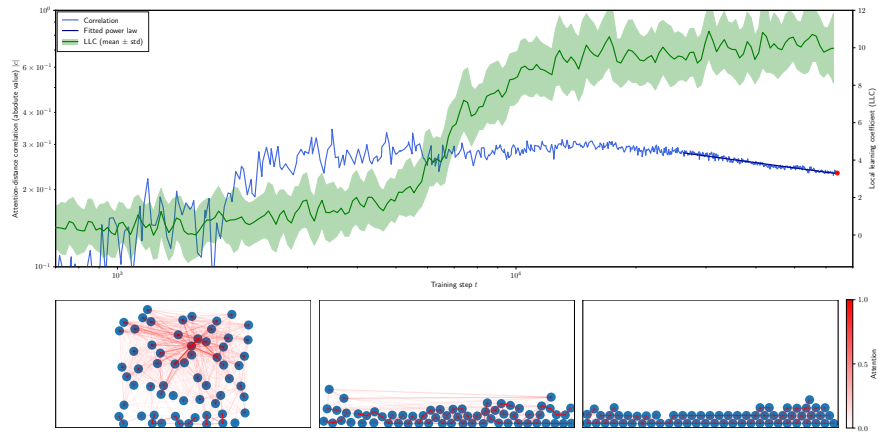


Figure 23: Attention-distance correlation and local learning coefficient results for head 3-6 in training run 1. The fitted curve is $\log(|c|) = -0.210 \log(t) + 0.879$ with $R^2 = 0.932$ (see Table 5).

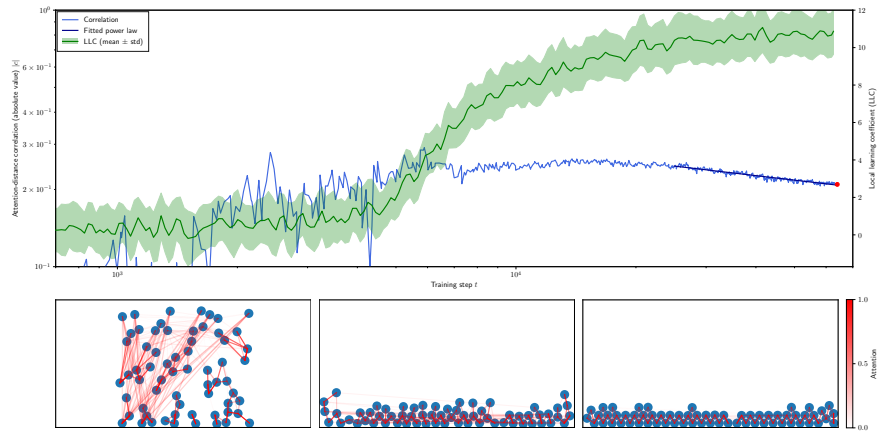


Figure 24: Attention-distance correlation and local learning coefficient results for head 2-0 in training run 2. The fitted curve is $\log(|c|) = -0.182 \log(t) + 0.438$ with $R^2 = 0.923$ (see Table 5).

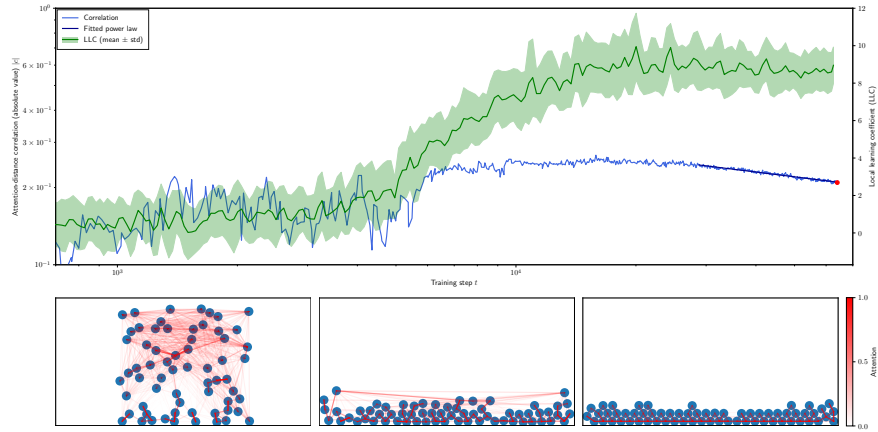


Figure 25: Attention-distance correlation and local learning coefficient results for head 3-0 in training run 2. The fitted curve is $\log(|c|) = -0.193 \log(t) + 0.574$ with $R^2 = 0.954$ (see Table 5).

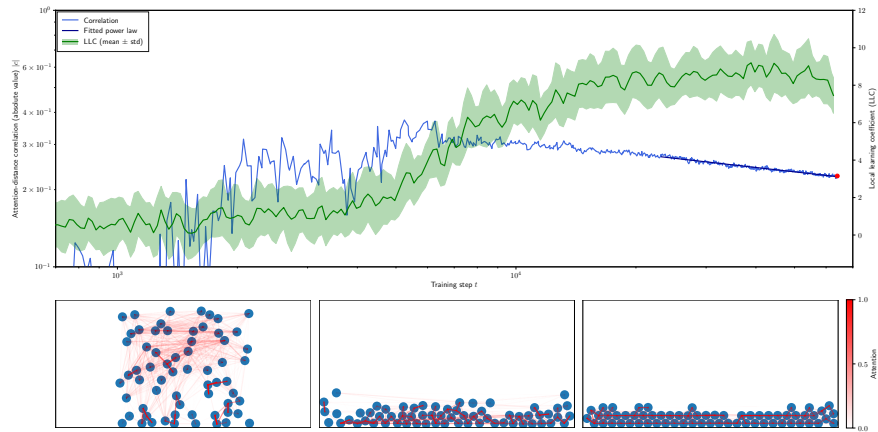


Figure 26: Attention-distance correlation and local learning coefficient results for head 3-1 in training run 2. The fitted curve is $\log(|c|) = -0.175 \log(t) + 0.448$ with $R^2 = 0.947$ (see Table 5).

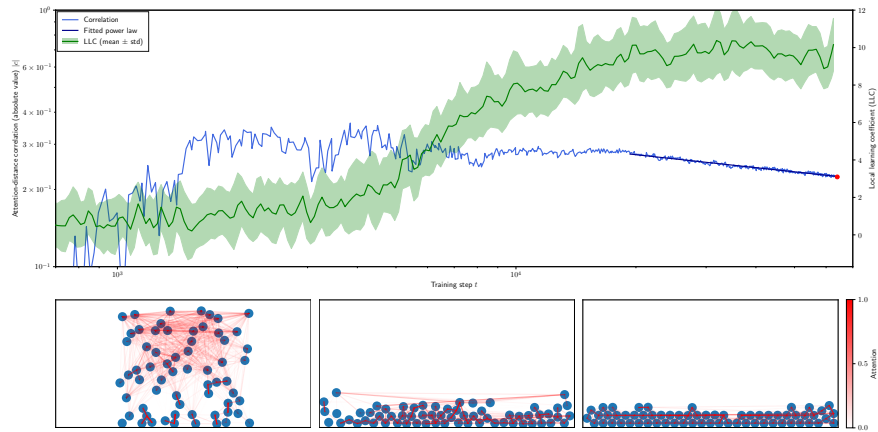


Figure 27: Attention-distance correlation and local learning coefficient results for head 3-6 in training run 2. The fitted curve is $\log(|c|) = -0.168 \log(t) + 0.364$ with $R^2 = 0.964$ (see Table 5).

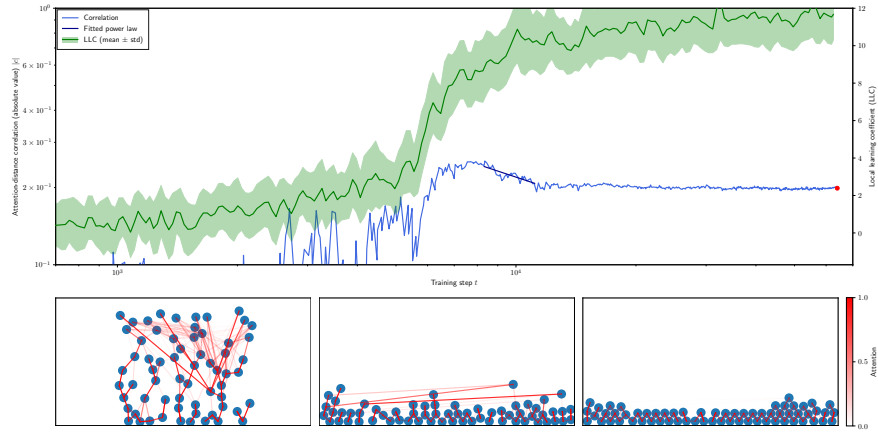


Figure 28: Attention-distance correlation and local learning coefficient results for head 2-2 in training run 3. The fitted curve is $\log(|c|) = -0.516 \log(t) + 3.240$ with $R^2 = 0.715$ (see Table 5).

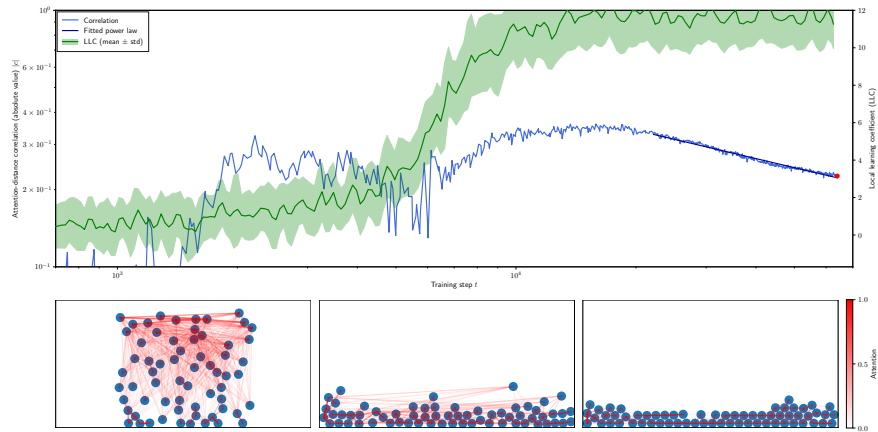


Figure 29: Attention-distance correlation and local learning coefficient results for head 3-2 in training run 3. The fitted curve is $\log(|c|) = -0.367 \log(t) + 2.559$ with $R^2 = 0.982$ (see Table 5).

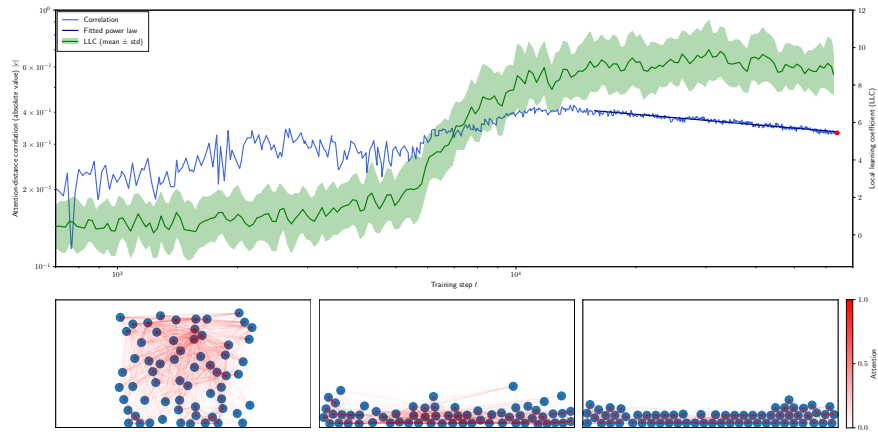


Figure 30: Attention-distance correlation and local learning coefficient results for head 3-3 in training run 3. The fitted curve is $\log(|c|) = -0.135 \log(t) + 0.405$ with $R^2 = 0.936$ (see Table 5).

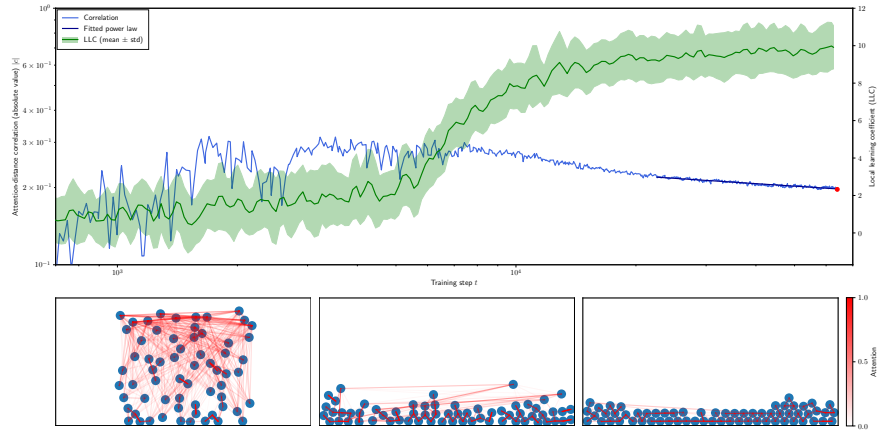


Figure 31: Attention-distance correlation and local learning coefficient results for head 3-6 in training run 3. The fitted curve is $\log(|c|) = -0.101 \log(t) - 0.505$ with $R^2 = 0.904$ (see Table 5).

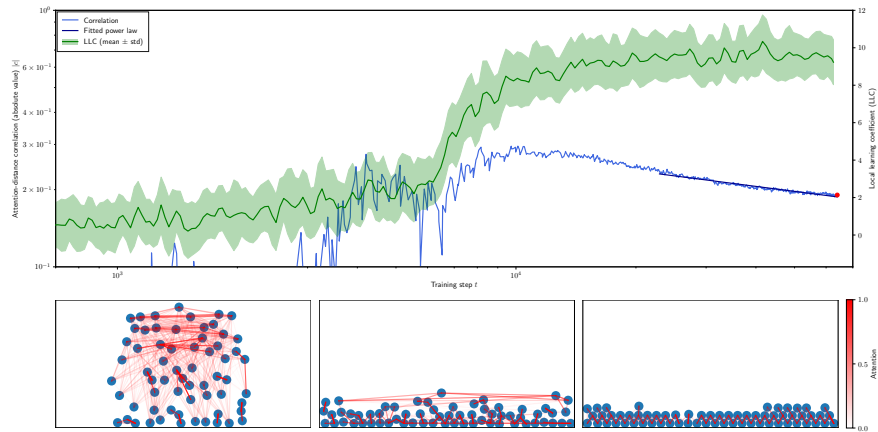


Figure 32: Attention-distance correlation and local learning coefficient results for head 3-1 in training run 4. The fitted curve is $\log(|c|) = -0.201 \log(t) + 0.545$ with $R^2 = 0.953$ (see Table 5).

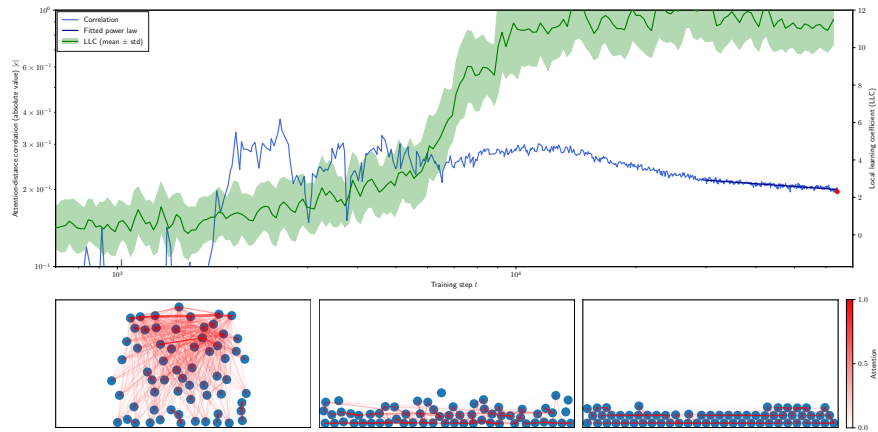


Figure 33: Attention-distance correlation and local learning coefficient results for head 3-2 in training run 4. The fitted curve is $\log(|c|) = -0.110 \log(t) - 0.394$ with $R^2 = 0.775$ (see Table 5).

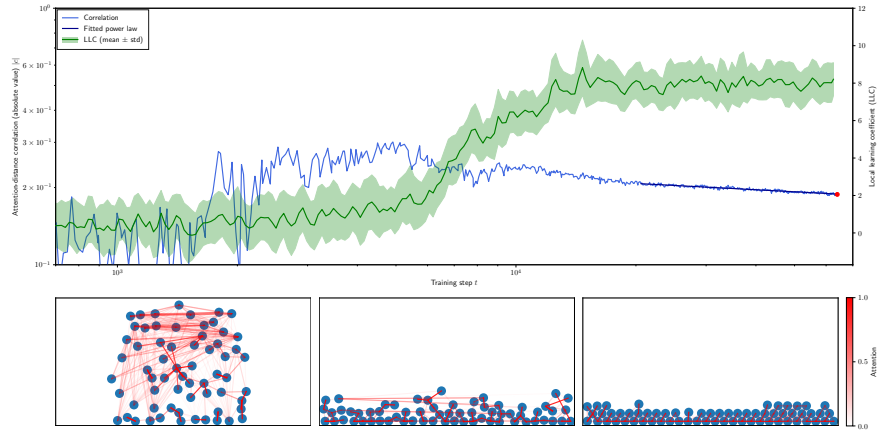


Figure 34: Attention-distance correlation and local learning coefficient results for head 3-5 in training run 4. The fitted curve is $\log(|c|) = -0.082 \log(t) - 0.760$ with $R^2 = 0.911$ (see Table 5).

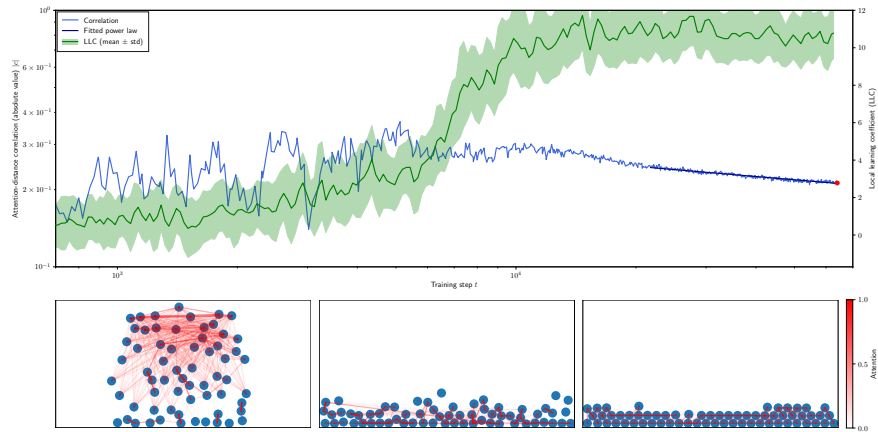


Figure 35: Attention-distance correlation and local learning coefficient results for head 3-7 in training run 4. The fitted curve is $\log(|c|) = -0.132 \log(t) - 0.094$ with $R^2 = 0.930$ (see Table 5).